

Probing Tissue Microarchitecture of the Baby Brain via Spherical Mean Spectrum Imaging

Khoi Minh Huynh[†], Tiantian Xu[†], Ye Wu[†], Xifeng Wang, Geng Chen, Kim-Han Thung, Haiyong Wu, Weili Lin, Dinggang Shen, and Pew-Thian Yap*

Abstract

During the first years of life, the human brain undergoes dynamic spatially-heterogeneous changes, involving differentiation of neuronal types, dendritic arborization, axonal ingrowth, outgrowth and retraction, synaptogenesis, and myelination. To better quantify these changes, this article presents a method for probing tissue microarchitecture by characterizing water diffusion in a *spectrum* of length scales, factoring out the effects of intra-voxel orientation heterogeneity. Our method is based on the spherical means of the diffusion signal, computed over gradient directions for a set of diffusion weightings (i.e., *b*-values). We decompose the spherical mean profile at each voxel into a spherical mean spectrum (SMS), which essentially encodes the fractions of spin packets undergoing fine- to coarse-scale diffusion processes, characterizing restricted and hindered diffusion stemming respectively from intra- and extra-cellular water compartments. From the SMS, multiple orientation distribution invariant indices can be computed, allowing for example the quantification of neurite density, microscopic fractional anisotropy (μ FA), per-axon axial/radial diffusivity, and free/restricted isotropic diffusivity. We show that these indices can be computed for the developing brain for greater sensitivity and specificity to development related changes in tissue microstructure. Also, we demonstrate that our method, called spherical mean spectrum imaging (SMSI), is fast, accurate, and can overcome the biases associated with other state-of-the-art microstructure models.

Index Terms

Diffusion Magnetic Resonance Imaging (DMRI), Spherical Mean Spectrum (SMS), Pediatric Imaging, Brain Tissue Microstructure

Copyright (c) 2020 IEEE. Personal use of this material is permitted. Permission from IEEE must be obtained for all other uses, in any current or future media, including reprinting/republishing this material for advertising or promotional purposes, creating new collective works, for resale or redistribution to servers or lists, or reuse of any copyrighted component of this work in other works.

This work was supported in part by NIH grants (NS093842, EB022880, MH104324, and MH110274) and the efforts of the UNC/UMN Baby Connectome Project Consortium.

K.M. Huynh, T. Xu, Y. Wu, G. Chen, W. Lin, D. Shen, and P.-T. Yap are with the Department of Radiology and Biomedical Research Imaging Center (BRIC), University of North Carolina at Chapel Hill, NC, U.S.A. K.M. Huynh, D. Shen, and P.-T. Yap are also with the Department of Biomedical Engineering, University of North Carolina at Chapel Hill, NC, U.S.A. H. Wu is with School of Information Engineering, Xiaozhuang University, Nanjing, China. X. Wang is with Department of Biostatistics, University of North Carolina at Chapel Hill, North Carolina, U.S.A.

[†]Khoi Minh Huynh, Tiantian Xu, and Ye Wu contributed equally to this work.

Corresponding author: Pew-Thian Yap (ptyap@med.unc.edu)

I. INTRODUCTION

Biophysical diffusion models play a vital role in characterizing complex changes in tissue microstructure, such as dendrites, axons, and glial cells, in the developing brain, giving important insights into the structural basis of the human brain. Microstructural analysis of the human brain has revealed important information on the maturational processes that occur in newborns [1].

Diffusion tensor imaging (DTI) is commonly used to assess microstructural changes in the human brain. DTI indices such as mean, radial, and axial diffusivities (MD, RD, AD), and fractional anisotropy (FA) can be used as quantitative indicators of brain developmental changes. However, DTI does not differentiate between white matter intra- and extra-axonal compartments. Moreover, FA can only measure voxel-level anisotropy, which mingles the effects of neurite microscopic-level anisotropy and orientation dispersion [2].

Considerable efforts have been dedicated to deriving suitable diffusion indices to probe tissue microstructural properties. Assaf and Basser [3] introduced the composite hindered and restricted model of diffusion (CHARMED) to address the deficiencies of DTI. This framework was later extended in [4] using a model called AxCaliber to estimate the axon diameter distribution. Alexander et al. introduced orientationally invariant indices of axon diameter using a four-compartment tissue model combined with an optimized multi-shell acquisition scheme [5]. Using diffusion kurtosis imaging (DKI), Fieremans et al. [6] probed restricted water diffusion using two non-exchanging compartments representing intra- and extra-axonal spaces. Taking a step forward, Zhang et al. [7] introduced NODDI to quantify neurite orientation density and dispersion. Daducci et al. [8] presented AMICO to significantly decrease NODDI computation time by linearizing the fitting problem. White et al. [9] demonstrated how restriction spectrum imaging (RSI), which involves a straightforward extension of the linear spherical deconvolution (SD) model [10, 11], can be used to probe tissue orientation structures over a spectrum of length scales with minimal assumptions on the underlying microarchitecture. Kaden et al. [12] presented the spherical mean technique (SMT) method for estimating per-axon microscopic features, not confounded by the effects of fiber crossing and dispersion. SMT was extended in [13] to take into consideration the presence of multiple compartments (MC-SMT). DIAMOND [14] is based on a tridimensional extension of the statistical model of the apparent diffusion coefficient [15] and characterizes microstructural diffusivity with consideration of intra-voxel heterogeneities. Diffusion basis spectrum imaging (DBSI) [16] characterizes water diffusion by considering the diffusion signal as a linear combination of multiple anisotropic tensors and a spectrum of isotropic diffusion tensors.

The infant brain develops rapidly in terms of total brain volume and tissue microarchitecture. The MR signal reflects the effects of various biological factors associated with maturation-related changes [17]. To quantify these changes, existing studies mostly focus on the grey-white matter contrast given by T1- and T2-weighted images, diffusion indices given by DTI (e.g., FA and apparent diffusion coefficient (ADC)) [18], and major fascicles in the infant brain [19]. DTI has been used to show white matter changes in preterm infants [18, 20, 21, 22] and for investigating brain-behavior relationships and maturation in infant white matter bundles [19, 23, 24].

With the advanced microstructural analysis methods described previously, distinct properties, such as neurite density, axon diameter, and orientation dispersion of the developing brain can be quantified. Kunz et al. [1] applied

CHARMED and NODDI to study the maturation processes of newborn brains. Jelescu et al. [25] studied the microstructural changes in the infant brain using DKI and NODDI. Both models reveal a non-linear increase in intra-axonal water fraction and in tortuosity of the extra-axonal space as a function of age in the genu and splenium of the corpus callosum and the posterior limb of the internal capsule. Neurite density estimated using NODDI combined with myelin content information can be used to obtain the myelin g -ratio, which is a reliable measure of axonal myelination defined as the ratio of the inner axonal diameter to the total outer diameter [26].

The aforementioned approaches are limited in that they (i) assume a predefined number of compartments (e.g., CHARMED, MC-SMT, SMT, NODDI), (ii) fix the diffusivity of one or more compartments (e.g., NODDI, RSI), or (iii) model only a portion of the diffusion spectrum (e.g., DBSI, RSI). Given the complex tissue microstructure [27] and its dynamic developmental changes [28, 29], such assumptions are not necessarily ideal for accurate characterization of microstructural properties. To better quantify the changes in the developing brain by tackling the mentioned problems, we present in this article a method for probing tissue microarchitecture by characterizing water diffusion with a full *spectrum* of diffusion shapes and scales and at the same time factoring out the effects of intra-voxel orientation dispersion. Our method is based on the spherical means of the diffusion signal, computed over gradient directions for a set of diffusion weightings [12, 13, 30]. We decompose the spherical mean profile at each voxel into a spherical mean spectrum (SMS), which encodes the fractions of spin packets undergoing fine- to coarse-scale diffusion processes. From the SMS, multiple rotation invariant indices can be computed for greater sensitivity and specificity to changes in tissue microstructure.

II. METHOD

In this section, we will first provide a brief summary of SMT [12, 13] and then describe our method, called spherical mean spectrum imaging (SMSI), the implementation details, and the associated diffusion indices.

A. Spherical Mean Technique (SMT)

Spherical mean technique (SMT) [12] estimates per-axon parallel and perpendicular diffusivities by factoring out the effects of orientation dispersion. It is based on the observation that the spherical mean of the diffusion-attenuated signal over the gradient directions g , i.e.,

$$\bar{S}_b = \frac{1}{4\pi} \int_{g \in \mathbb{S}^2} S_b(g) dg \quad (1)$$

does not depend on the fiber orientation distribution. Assuming that the signal can be represented as the spherical convolution of a fiber orientation distribution function (fODF) $p(\omega)$ ($p(\omega) \geq 0$, $\int_{\mathbb{S}^2} p(\omega) d\omega = 1$, $p(\omega) = p(-\omega)$, $\omega \in \mathbb{S}^2$) with an axial and antipodal symmetric kernel $h_b(g|\omega) = h_b(\omega|g) \equiv h_b(|\langle g, \omega \rangle|)$, i.e.,

$$S_b(g) = S_0 \int_{\omega \in \mathbb{S}^2} h_b(g|\omega) p(\omega) d\omega, \quad (2)$$

it can be shown that

$$\bar{S}_b = S_0 \bar{h}_b, \quad (3)$$

where \bar{h}_b is the kernel spherical mean.

Setting the kernel as an axial symmetric diffusion tensor [31], which is parameterized by orientation ω , parallel diffusivity λ_{\parallel} , and perpendicular diffusivity λ_{\perp} , i.e.,

$$\begin{aligned} h_b(g|\omega, \lambda_{\parallel}, \lambda_{\perp}) &= \underbrace{\exp(-b\langle g, \omega \rangle^2 \lambda_{\parallel})}_{\text{longitudinal}} \underbrace{\exp(-b(1 - \langle g, \omega \rangle^2) \lambda_{\perp})}_{\text{transverse}} \\ &= \exp(-b\lambda_{\perp}) \exp(-b(\lambda_{\parallel} - \lambda_{\perp})\langle g, \omega \rangle^2), \end{aligned} \quad (4)$$

it is straightforward, by noting

$$\bar{h}_b = \int_{g \in \mathbb{S}^2} h_b(g|\omega) dg = \int_0^1 h_b(x) dx, \quad x \equiv \langle g, \omega \rangle \quad (5)$$

$$\text{erf}(x) = \frac{2}{\sqrt{\pi}} \int_0^x \exp(-t^2) dt, \quad (6)$$

to show that

$$\bar{h}_b(\lambda_{\parallel}, \lambda_{\perp}) = \frac{1}{4\pi} \int_{g \in \mathbb{S}^2} h_b(g|\omega, \lambda_{\parallel}, \lambda_{\perp}) dg \quad (7)$$

$$= \exp(-b\lambda_{\perp}) \frac{\sqrt{\pi} \text{erf}(\sqrt{b(\lambda_{\parallel} - \lambda_{\perp})})}{2\sqrt{b(\lambda_{\parallel} - \lambda_{\perp})}}. \quad (8)$$

Note that \bar{h}_b is not dependent on ω . In SMT, the above equation is substituted in (3) to solve for λ_{\parallel} and λ_{\perp} :

$$\frac{\bar{S}_b}{S_0} = \begin{cases} \exp(-b\lambda_{\perp}), & \lambda_{\perp} = \lambda_{\parallel}, \\ \exp(-b\lambda_{\perp}) \frac{\sqrt{\pi} \text{erf}(\sqrt{b(\lambda_{\parallel} - \lambda_{\perp})})}{2\sqrt{b(\lambda_{\parallel} - \lambda_{\perp})}}, & \lambda_{\perp} < \lambda_{\parallel}. \end{cases} \quad (9)$$

B. Spherical Mean Spectrum Imaging (SMSI)

1) *Ensemble of Spin Packets:* We assume the signal measurements at each voxel to be a collective outcome of an ensemble of homogeneous spin packets originating from different positions within the voxel, each undergoing local anisotropic or isotropic diffusion represented by an axial-symmetric diffusion tensor model and contributes to the signal for gradient direction g by $h_b(g|\omega, \lambda_{\parallel}, \lambda_{\perp})$ [15]. Bigger heterogeneous spin packets, such as those assumed in [14], can be decomposed into smaller homogeneous ones. The diffusion patterns of the spin packets are determined by microstructural barriers in intra- and extra-cellular spaces. Encoding the fractions of the spin packets using probability distribution $p(\omega, \lambda_{\parallel}, \lambda_{\perp})$, the diffusion-attenuated signal S can be written as

$$S_b(g) = S_0 \int_{\omega, \lambda_{\parallel}, \lambda_{\perp}} p(\omega, \lambda_{\parallel}, \lambda_{\perp}) h_b(g|\omega, \lambda_{\parallel}, \lambda_{\perp}) d\omega d\lambda_{\parallel} d\lambda_{\perp}. \quad (10)$$

Computing the spherical mean of the signal results in

$$\bar{S}_b = S_0 \int_{\omega, \lambda_{\parallel}, \lambda_{\perp}} p(\omega, \lambda_{\parallel}, \lambda_{\perp}) \bar{h}_b(\lambda_{\parallel}, \lambda_{\perp}) d\omega d\lambda_{\parallel} d\lambda_{\perp}. \quad (11)$$

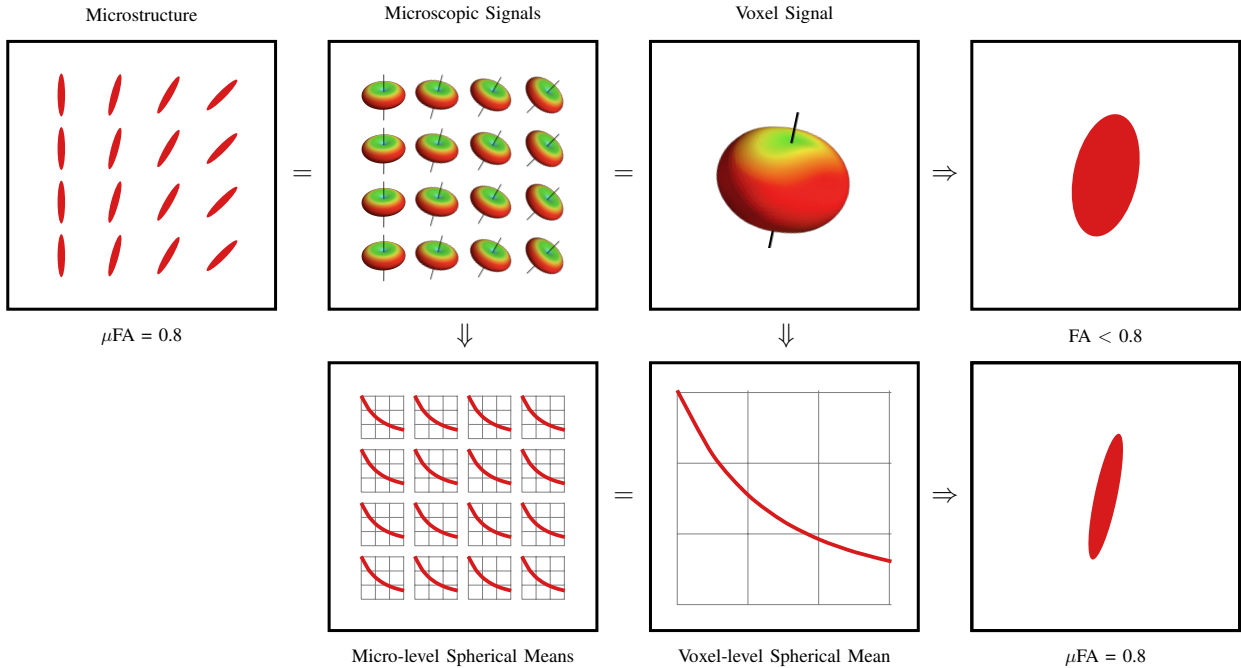


Fig. 1. **Spherical Mean & Microstructure.** The spherical mean can be used to quantify the diffusion patterns of spin packets in microenvironments, unconfounded by the orientation distribution. Unlike microscopic FA (μ FA), voxel-level DTI-FA underestimates the anisotropy due to orientation dispersion.

The variable ω can be marginalized out, giving

$$\bar{S}_b = S_0 \int_{\lambda_{\parallel}, \lambda_{\perp}} p(\lambda_{\parallel}, \lambda_{\perp}) \bar{h}_b(\lambda_{\parallel}, \lambda_{\perp}) d\lambda_{\parallel} d\lambda_{\perp}. \quad (12)$$

The spherical mean signal of each voxel can thus be seen as the weighted combination of the spherical mean signals of the spin packets. Note that in the derivation, the antipodal symmetry assumption of the fiber orientation distributions is not needed. If the spin packets can be represented by a single set of diffusivities $(\lambda_{\parallel}^*, \lambda_{\perp}^*)$, $p(\lambda_{\parallel}, \lambda_{\perp})$ can be defined using the delta function, i.e., $p(\lambda_{\parallel}, \lambda_{\perp}) = \delta(\lambda_{\parallel} - \lambda_{\parallel}^*) \delta(\lambda_{\perp} - \lambda_{\perp}^*)$, giving $\bar{S}_b = S_0 \bar{h}_b(\lambda_{\parallel}^*, \lambda_{\perp}^*)$, which is identical to (3) of SMT. Fig. 1 illustrates how the spherical mean can be used to quantify microstructural properties. We name $p(\lambda_{\parallel}, \lambda_{\perp})$ the spherical mean spectrum (SMS) because it encodes the probability of diffusivity pairs $(\lambda_{\parallel}, \lambda_{\perp})$ according to the spherical mean profile.

2) *Spherical Mean Spectrum (SMS)*: We relax the assumption of SMT and introduce a method to estimate the SMS, $p(\lambda_{\parallel}, \lambda_{\perp})$, directly without imposing any constraints that restrict its shape. By studying the SMS (see Fig. 2), we can for example examine the fractions of spin packets undergoing isotropic ($\lambda_{\parallel} = \lambda_{\perp}$) or anisotropic ($\lambda_{\parallel} > \lambda_{\perp}$) diffusion and separate anisotropic diffusion into restricted (small λ_{\perp}) and hindered (larger λ_{\perp}) diffusion. Similar to RSI [9], the SMS allows us to probe tissue microarchitecture using a spectrum of diffusion scales. Dissimilar to RSI, the SMS is invariant to the fODF and is therefore well suited for regions with complex axonal geometries such as fanning and bending [32].

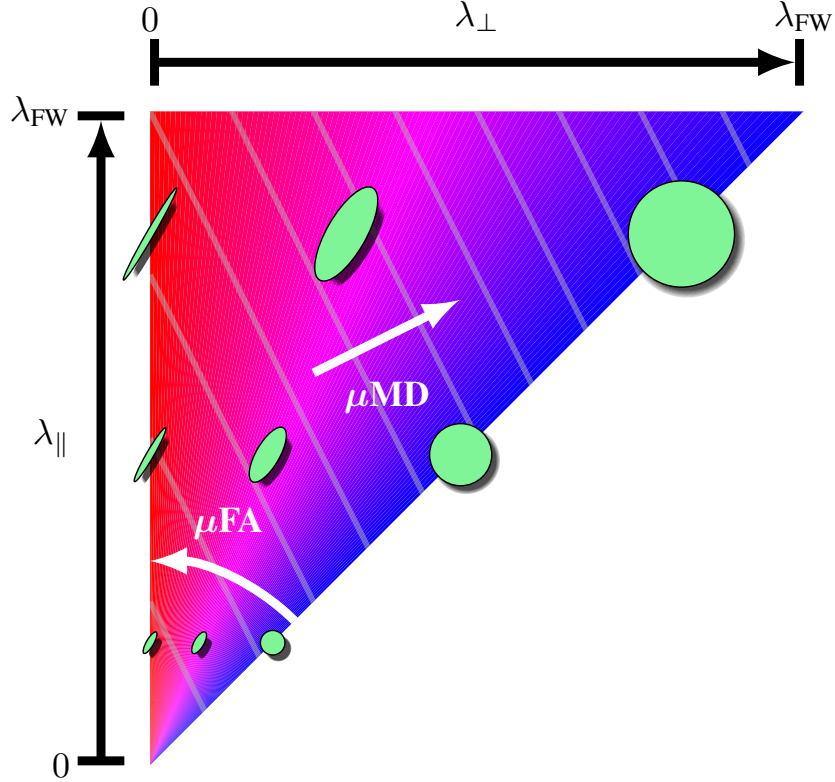


Fig. 2. **Spherical Mean Spectrum (SMS)**. The SMS map with constraint $0 < \lambda_{\perp} < \lambda_{\parallel} < \lambda_{\text{FW}}$. μFA ranges from 0 at the blue extreme to 1 at the red extreme. μMD increases perpendicular to the gray lines, on which μMD is constant.

For the sake of feasibility, we discretize (12) by defining

$$p(\lambda_{\parallel}, \lambda_{\perp}) = \sum_i \nu[i] \delta(\lambda_{\parallel} - \lambda_{\parallel}[i]) \delta(\lambda_{\perp} - \lambda_{\perp}[i]) \quad (13)$$

to obtain

$$\bar{S}_b = S_0 \sum_i \nu[i] \bar{h}_b(\lambda_{\parallel}[i], \lambda_{\perp}[i]) \quad (14)$$

with volume fractions $\{\nu[1], \nu[2], \dots\}$. The ranges of $\lambda_{\parallel}[i]$ and $\lambda_{\perp}[i]$ are set according to constraint $0 < \lambda_{\perp}[i] < \lambda_{\parallel}[i] < \lambda_{\text{FW}}, \forall i$, where λ_{FW} is the diffusivity of free water (see Fig. 2). Note that since $\int_{\lambda_{\parallel}, \lambda_{\perp}} p(\lambda_{\parallel}, \lambda_{\perp}) d\lambda_{\parallel} d\lambda_{\perp} = 1$, we have $\sum_i \nu[i] = 1$.

Solving for ν using (14) is an ill-posed inverse problem since there are typically more unknowns than observations. With dictionary $A = [\bar{h}_b(\lambda_{\parallel}[1], \lambda_{\perp}[1]), \bar{h}_b(\lambda_{\parallel}[2], \lambda_{\perp}[2]), \dots] \in \mathbb{R}^{n \times p}$, where n is the number of b -shells and p is the number of dictionary atoms, we propose a solution based on elastic net [33]:

$$\nu = \underset{\nu \geq 0}{\text{arg min}} \|A\nu - \bar{S}\|_2^2 + \gamma_1 \|\text{diag}(w)\nu\|_1 + \gamma_2 \|\nu\|_2^2, \quad (15)$$

where the first term ensures data fidelity, and γ_1 and γ_2 control the lasso (ℓ_1 -norm) penalty and ridge (ℓ_2 -norm) penalty, respectively. \bar{S} is a vector containing the spherical means $\{\bar{S}_b\}$ for different b -shells. w is a weight vector.

The reasons for elastic net are as follows:

- 1) Sparsity — Ridge penalization keeps all atoms in the model and is hence not parsimonious. Lasso penalization promotes sparse solutions and hence improves interpretability.
- 2) Stability — If the atoms are highly correlated, lasso tends to select only one of them indiscriminately. Elastic net has the ability to select ‘grouped’ predictors, a property that is not shared by lasso.
- 3) Super-resolution — Lasso selects at most n atoms before it saturates. Elastic net can be seen a stabilized version of lasso and can be written as an augmented problem [33]:

$$\nu = \underset{\nu \geq 0}{\operatorname{arg\,min}} \left\| \begin{pmatrix} A \\ \sqrt{\gamma_2} I \end{pmatrix} \nu - \begin{pmatrix} \bar{S} \\ 0 \end{pmatrix} \right\|_2^2 + \gamma_1 \|\operatorname{diag}(w)\nu\|_1, \quad (16)$$

allowing it to potentially select all p atoms in all situations. This property was also used in [11] to improve estimation of fiber orientation distributions.

Fig. 3 illustrates how SMSI determines the microstructural compartments.

3) *Diffusion Indices*: We divide the SMS into three compartments: isotropic, hindered, and restricted. Note that this is based on compartments commonly used in the literature, but is not the only way to divide the SMS. Also, each compartment can be represented by multiple, instead of one, diffusion kernels. It is assumed that on the timescale of a typical diffusion experiment, the effects of tissue membrane permeability is negligible. This is necessary in order to enforce strict signal compartmentalization. The isotropic diffusion compartment is represented by atoms with $\lambda_{\parallel} = \lambda_{\perp}$ and a spectrum of diffusivity ranging from 0 to 3 mm²/s, similar to [16]. The hindered and restricted compartments are anisotropic with $\lambda_{\parallel} > \lambda_{\perp}$. We define the restricted compartment with $\frac{\lambda_{\parallel}}{\lambda_{\perp}} \geq \tau^2$ and the hindered compartment with $\frac{\lambda_{\parallel}}{\lambda_{\perp}} < \tau^2$, where τ is the geometric tortuosity [9]. Bihan suggested a value of $\frac{\pi}{2} \approx 1.57$ for τ [34]. The perpendicular diffusivity of the restricted compartment is 0 in [13], corresponding to $\tau \rightarrow \infty$. We determine τ automatically via grid search based on the voxels in the body of the corpus callosum, where fiber dispersion and isotropic diffusion contamination are low, by exploring all possible values of τ estimated via MC-SMT. We found that τ is typically 2.6 for the Human Connectome Project (HCP) and Baby Connectome Project (BCP) datasets. In practice, λ_{\perp} reflects the combined effects of nonvanishing permeability and possibly water in the extra-cellular space experiencing cylindrical diffusion symmetry [35]. Intra-axonal diffusion is restricted and extra-axonal diffusion is hindered [13, 36].

Microscopic Anisotropy — We present here a new measure of microscopic anisotropy for multi-compartmental models. We note that the orientations of the tensors used to represent the spin-packets in the microenvironments are between totally coherent with no dispersion and totally incoherent with full dispersion in all directions. For full dispersion, we have $p(\omega, \lambda_{\parallel}, \lambda_{\perp}) = p(\omega)p(\lambda_{\parallel}, \lambda_{\perp}) = \frac{1}{4\pi}p(\lambda_{\parallel}, \lambda_{\perp})$. Therefore, it is straightforward to show from

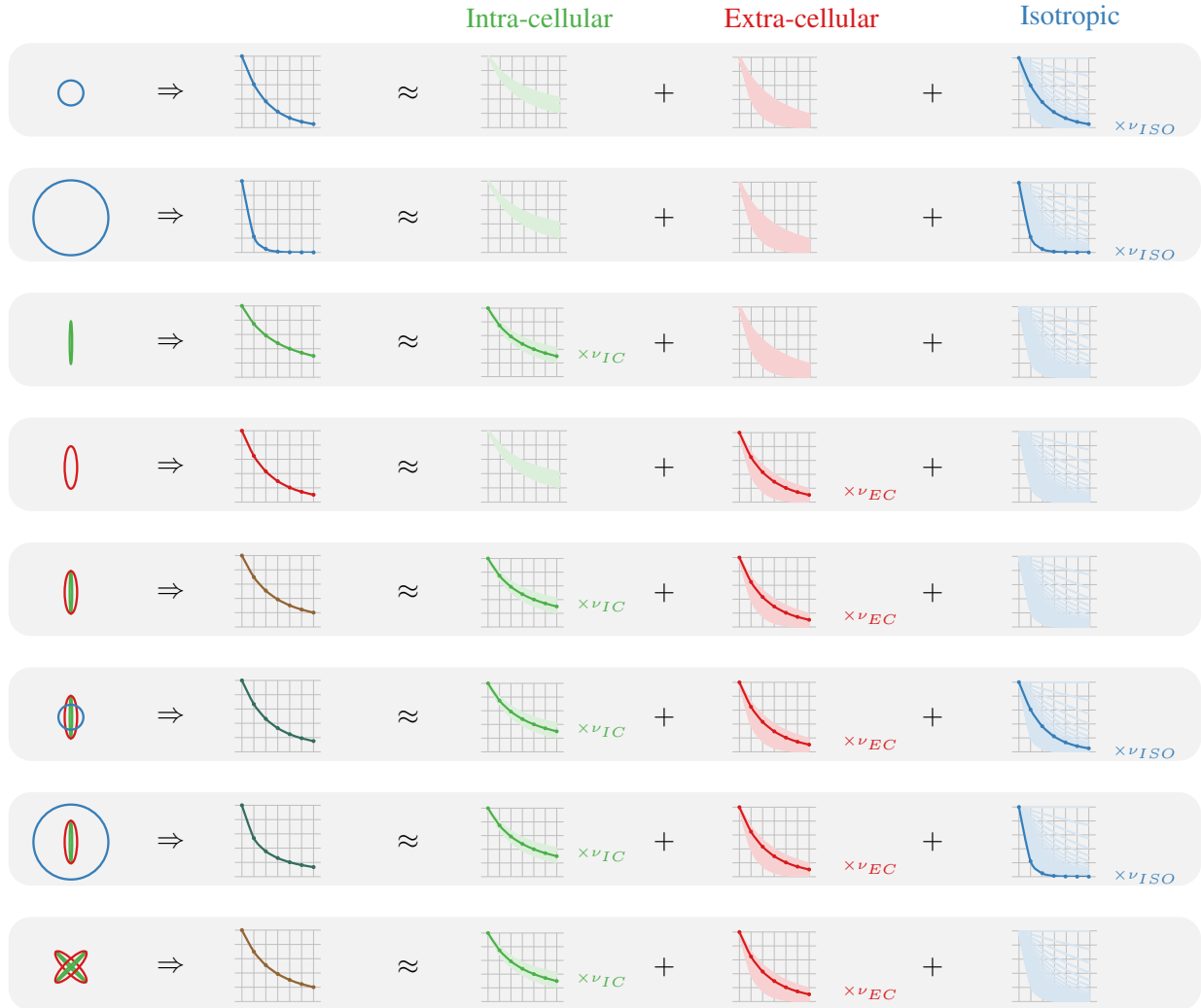


Fig. 3. **SMSI Overview.** Tissue compartments (first column) and their respective spherical mean signals (second column). SMSI determines the associated atoms and the respective volume fractions (ν). The atoms can be groups into restricted intra-cellular (green), hindered extra-cellular (red), and isotropic (blue) diffusion compartments. Note that SMSI is robust to crossing fibers (e.g., compare the fifth and last rows).

(10) that the signal resulting from this configuration is actually the spherical mean \bar{S}_b :

$$\begin{aligned}
 S_b(g) &= S_0 \int_{\omega, \lambda_{\parallel}, \lambda_{\perp}} \frac{1}{4\pi} p(\lambda_{\parallel}, \lambda_{\perp}) h_b(g|\omega, \lambda_{\parallel}, \lambda_{\perp}) d\omega d\lambda_{\parallel} d\lambda_{\perp} \\
 &= S_0 \int_{\lambda_{\parallel}, \lambda_{\perp}} p(\lambda_{\parallel}, \lambda_{\perp}) \bar{h}_b(\lambda_{\parallel}, \lambda_{\perp}) d\lambda_{\parallel} d\lambda_{\perp} \\
 &\approx S_0 \sum_i \nu[i] \bar{h}_b(\lambda_{\parallel}[i], \lambda_{\perp}[i]) \\
 &\approx \bar{S}_b.
 \end{aligned} \tag{17}$$

For no dispersion, the signal $S_b^{\uparrow}(g)$ is given by aligning the spin-packet tensors, i.e., $p(\omega, \lambda_{\parallel}, \lambda_{\perp}) = \delta(\omega -$

$\omega_0)p(\lambda_{\parallel}, \lambda_{\perp})$ for an arbitrary ω_0 :

$$\begin{aligned} S_b(g) &= S_0 \int_{\lambda_{\parallel}, \lambda_{\perp}} p(\lambda_{\parallel}, \lambda_{\perp}) h_b(g|\omega_0, \lambda_{\parallel}, \lambda_{\perp}) d\lambda_{\parallel} d\lambda_{\perp} \\ &\approx S_0 \sum_i \nu[i] h_b(g|\omega_0, \lambda_{\parallel}[i], \lambda_{\perp}[i]) \\ &= S_b^{\uparrow}(g). \end{aligned} \quad (18)$$

A measure of anisotropy of the spin-packets can be defined as

$$\frac{1}{4\pi} \sum_b \int_{\mathbb{S}^2} [S_b^{\uparrow}(g) - \bar{S}_b]^2 dg. \quad (19)$$

We normalize (19) with the maximum anisotropy, which happens when we set for all anisotropic terms $\lambda_{\perp}[i] = 0$. Denoting the signal and mean in this case respectively as $S_b^{\uparrow,*}(g)$ and \bar{S}_b^* , the microscopic anisotropy index (MAI) is defined as

$$\text{MAI} = \sqrt{\frac{\sum_b \int_{\mathbb{S}^2} [S_b^{\uparrow}(g) - \bar{S}_b]^2 dg}{\sum_b \int_{\mathbb{S}^2} [S_b^{\uparrow,*}(g) - \bar{S}_b^*]^2 dg}}. \quad (20)$$

Similar to FA, MAI ranges from 0 to 1. Note that MAI is free from the influence of dispersion and can be used for multi-compartmental models, including SMSI, SMT, MC-SMT, and NODDI, provided that the diffusivities and volume fractions of the compartments are known.

Orientation Coherence — In case of full dispersion, orientation coherence is minimal and should correspond to a value of zero. We measure orientation coherence as the distance between the observed signal and the full dispersion signal:

$$\frac{1}{4\pi} \sum_b \int_{\mathbb{S}^2} [S_b(g) - \bar{S}_b]^2 dg. \quad (21)$$

We normalize the coherence with the maximum coherence when there is no dispersion, giving the orientation coherence index (OCI):

$$\begin{aligned} \text{OCI} &= \sqrt{\frac{[\frac{1}{4\pi} \sum_b \int_{\mathbb{S}^2} [S_b(g) - \bar{S}_b]^2 dg - \sigma^2]_+}{\frac{1}{4\pi} \sum_b \int_{\mathbb{S}^2} [S_b^{\uparrow}(g) - \bar{S}_b]^2 dg}} \\ &\approx \sqrt{\frac{[\sum_b \int_{\mathbb{S}^2} [S_b(g) - \bar{S}_b]^2 dg - k\sigma^2]_+}{\sum_b \int_{\mathbb{S}^2} [S_b^{\uparrow}(g) - \bar{S}_b]^2 dg}}, \end{aligned} \quad (22)$$

where σ is the noise standard deviation, which can be computed via maximum likelihood estimation using a set of b_0 images [12], and k is the total number of gradient directions across all shells. Operator $[z]_+$ returns z if $z \geq 0$ and 0 otherwise. OCI ranges from 0 for no coherence (full dispersion) to 1 for full coherence (no dispersion). Similar to MAI, the OCI definition is general and compatible among different models. The relationship between MAI, OCI, and orientation heterogeneity is illustrated in Fig. 4.

Isotropic Diffusion Elimination — Isotropic diffusion signal can be removed to increase sensitivity to axonal changes [37]. This is done for example via free-water elimination (FWE) indices [37]. RSI models both free-water diffusivity, estimated from intra-ventricular space, and longitudinal diffusivity, estimated from white matter. SMSI allows not

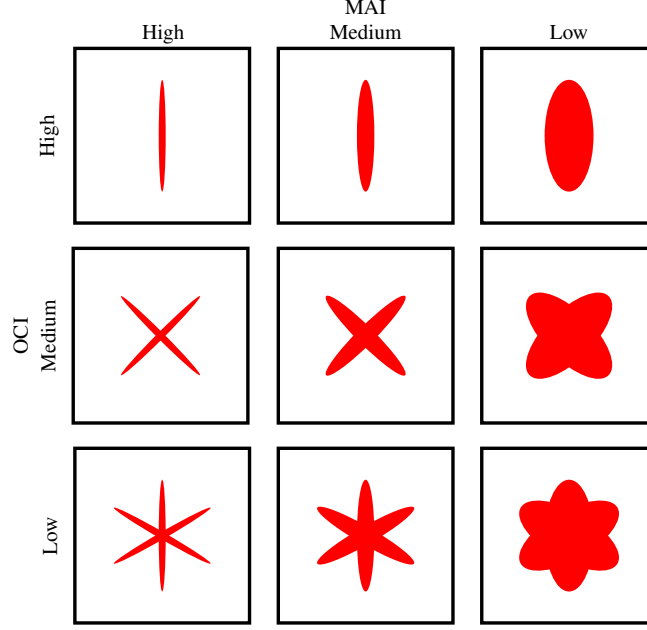


Fig. 4. **MAI and OCI.** MAI is sensitive to diffusion anisotropy but not orientation dispersion. OCI is sensitive to orientation heterogeneity.

TABLE I
SMSI INDICES.

Description	Indices	Description	Indices
Anisotropic VF	$v_a = \sum_{i \in \mathcal{A}} \nu[i]$	Intra-cellular AD	$\mu\text{AD}_{\text{ic}} = \frac{\sum_{i \in \mathcal{R}} \nu[i] \lambda_{\parallel}[i]}{\sum_{i \in \mathcal{R}} \nu[i]}$
Intra-cellular VF	$v_{\text{ic}} = \frac{\sum_{i \in \mathcal{R}} \nu[i]}{v_a}$	Intra-cellular RD	$\mu\text{RD}_{\text{ic}} = \frac{\sum_{i \in \mathcal{R}} \nu[i] \lambda_{\perp}[i]}{\sum_{i \in \mathcal{R}} \nu[i]}$
Extra-cellular VF	$v_{\text{ec}} = \frac{\sum_{i \in \mathcal{H}} \nu[i]}{v_a}$	Extra-cellular AD	$\mu\text{AD}_{\text{ec}} = \frac{\sum_{i \in \mathcal{H}} \nu[i] \lambda_{\parallel}[i]}{\sum_{i \in \mathcal{H}} \nu[i]}$
Isotropic VF	$v_{\text{iso}} = \sum_{i \in \mathcal{I}} \nu[i]$	Extra-cellular RD	$\mu\text{RD}_{\text{ec}} = \frac{\sum_{i \in \mathcal{H}} \nu[i] \lambda_{\perp}[i]}{\sum_{i \in \mathcal{H}} \nu[i]}$
Microscopic AD	$\mu\text{AD} = \frac{\sum_i \nu[i] \lambda_{\parallel}[i]}{\sum_i \nu[i]}$	Microscopic anisotropy index	$\text{MAI} = \sqrt{\frac{\sum_b \int_{\mathcal{S}^2} [S_b^{\dagger}(g) - \bar{S}_b]^2 dg}{\sum_b \int_{\mathcal{S}^2} [S_b^{\dagger,*}(g) - \bar{S}_b^*]^2 dg}}$
Microscopic RD	$\mu\text{RD} = \frac{\sum_i \nu[i] \lambda_{\perp}[i]}{\sum_i \nu[i]}$	Orientation coherence index	$\text{OCI} \approx \sqrt{\frac{[\sum_b \int_{\mathcal{S}^2} [S_b(g) - \bar{S}_b]^2 dg - k\sigma^2]_{+}}{\sum_b \int_{\mathcal{S}^2} [S_b^{\dagger}(g) - \bar{S}_b]^2 dg}}$
Microscopic MD	$\mu\text{MD} = \frac{\mu\text{AD} + 2\mu\text{RD}}{3}$	Microscopic sphericity	$\mu C_s = \frac{\mu\text{RD}}{\mu\text{MD}}$
Microscopic FA	$\mu\text{FA} = \frac{\mu\text{AD} - \mu\text{RD}}{\sqrt{\mu\text{AD}^2 + 2\mu\text{RD}^2}}$	Microscopic linearity	$\mu C_l = \frac{\mu\text{AD} - \mu\text{RD}}{3\mu\text{MD}}$

VF: Volume fraction, AD/RD/MD: Axial/Radial/Mean diffusivity, FA: Fractional anisotropy

Trapped diffusion: $\mathcal{T} = \{i | \lambda_{\parallel}[i] = 0, \lambda_{\perp}[i] = 0\}$

Anisotropic diffusion: $\mathcal{A} = \{i | \lambda_{\parallel}[i] > \lambda_{\perp}[i]\}$, Isotropic diffusion: $\mathcal{I} = \{i | \lambda_{\parallel}[i] = \lambda_{\perp}[i]\}$

Restricted diffusion: $\mathcal{R} = \{i | \lambda_{\perp}[i] \tau^2 \leq \lambda_{\parallel}[i], i \in \mathcal{A}, \tau > 1\}$, Hindered diffusion: $\mathcal{H} = \{i | \lambda_{\perp}[i] \tau^2 > \lambda_{\parallel}[i], i \in \mathcal{A}, \tau > 1\}$

$S_b, S_b^{\dagger}(g)$ and \bar{S}_b are the DW signal, the DW signal when all components are orientationally aligned, and the mean signal; $S_b^{\dagger,*}(g)$ and \bar{S}_b^* are the aligned signal and its mean when all $\lambda_{\perp}[i] = 0$.

$S_b^{\dagger,\dagger}(g), \bar{S}_b^{\dagger}, S_b^{\dagger,*,\dagger}(g)$, and $\bar{S}_b^{*,\dagger}$ are $S_b^{\dagger}(g), \bar{S}_b, S_b^{\dagger,*}(g)$, and \bar{S}_b^* , respectively, without isotropic compartments.

k is the total number of gradient directions, σ is the noise standard deviation, and τ is the geometric tortuosity.

only free water but the whole isotropic diffusion spectrum to be discarded, resulting in isotropic diffusion eliminated (IDE) indices. This is similar in spirit to DBSI [16]. Table I lists the SMSI indices. IDE indices are marked by symbol †.

4) *Implementation Details*: The quantification of microstructure using the spherical mean is affected by degeneracy in the sense that the spherical mean signal given by an anisotropic micro-environment may be indistinguishable from that of multiple isotropic micro-environments [38]. We describe in the following the implementation details of SMSI and how the degeneracy can be resolved using the full direction-sensitized signal from which the spherical mean signal is derived.

Resolving Degeneracy via Full-Signal Spectrum (FSS) — The full signal, unlike the mean signal, is not ambiguous in distinguishing isotropic and anisotropic diffusion.

Letting $\mathcal{H}(\lambda_{\parallel}[i], \lambda_{\perp}[i])$ be the matrix of rotational spherical harmonics (SHs) of $h_b(g|\omega, \lambda_{\parallel}, \lambda_{\perp})$, \mathcal{Y}_L the spherical harmonics of even orders up to L , and φ_i the SH coefficients of the fODF corresponding to $h_b(g|\omega, \lambda_{\parallel}[i], \lambda_{\perp}[i])$, (10) can be discretized as [10]

$$\mathcal{S} \approx \sum_i \mathcal{H}(\lambda_{\parallel}[i], \lambda_{\perp}[i]) \mathcal{Y}_L \varphi_i = \mathcal{B} \Phi. \quad (23)$$

Similar to (16), \mathcal{B} can be seen as a dictionary matrix and Φ can be solved with Tikhonov regularization

$$\min_{\Phi} \left\| \begin{pmatrix} \mathcal{B} \\ \sqrt{\gamma_3} \text{diag}(w') \end{pmatrix} \Phi - \begin{pmatrix} \mathcal{S} \\ 0 \end{pmatrix} \right\|_2^2. \quad (24)$$

From Φ , the volume fraction of each compartment i is the 0-th order SH coefficient [9].

Isotropic diffusion can be represented by isotropically-distributed anisotropic tensors, causing ambiguity. We prevent this by solving (24) with weight vector w' set to one for all atoms, identifying degenerate anisotropic atoms with generalized fractional anisotropy [39] (GFA) smaller than 0.3, and reapplying (24) with higher penalization of the degenerate atoms. This is implemented by doubling the corresponding elements in w' . The volume fractions obtained are denoted as ν_{FSS} .

Estimation of Isotropic Compartments — We use b -shells with $b \leq 1000$ s/mm² for an initial estimation using (16) with w set to one for all atoms. This improves the estimation of isotropic volume fractions. The volume fractions obtained are denoted as ν_{SMS} .

Iterative Reweighting — We then solve for the volume fractions using all b -shells via an iterative re-weighted elastic net, where at the j -th iteration we have

$$\nu_j = \arg \min_{\nu_j \geq 0} \left\| \begin{pmatrix} A \\ \sqrt{\gamma_2} I \end{pmatrix} \nu_j - \begin{pmatrix} \bar{S} \\ 0 \end{pmatrix} \right\|_2^2 + \gamma_1 \|\text{diag}(w_j) \nu_j\|_1, \quad (25)$$

where $w_j[i] = \frac{1}{\xi + \nu_{j-1}[i]}$ with ξ being a constant and ν_0 the geometric mean of ν_{FSS} and ν_{SMS} . The volume fractions estimated in this step can be utilized to set w' in (24) for alternating estimation of ν_{FSS} and ν_{SMS} . However, we found that one round of estimation is sufficient to produce accurate results.

The regularization parameters γ_1 , γ_2 , and γ_3 affect the estimation significantly. We develop an adaptive framework to automatically select these parameters based on the data:

- 1) Select regions with “simple” microstructure (e.g., the body of the corpus callosum for anisotropic diffusion and the ventricles for isotropic diffusion). This can be done by selecting voxels with highest and lowest FA

values.

- 2) Perform SMSI estimation with initialization as described above in these regions using multiple combinations of γ_1 's, γ_2 's, and γ_3 's.
- 3) For each combination of γ 's, substitute the obtained values for per-axon radial (μRD) and axial diffusivity (μAD) into (9). The optimal parameters are selected as those that minimize the difference between the predicted and the observed spherical mean signals.

5) *Debiasing*: Diffusion MRI signal is affected by Rician noise, especially at high b -value where the noise floor dominates the signal [40]. To reduce potential effects of this noise-induced bias, we correct the measured signal using the following steps:

- 1) Estimate the noise level σ voxel-wise via maximum-likelihood estimation (MLE) using a set of b_0 images. This is based on the assumption that the SNR of the b_0 images is high and therefore the noise distribution is approximately Gaussian. Only signal with $S < 5\sigma$ goes through the subsequent debiasing steps.
- 2) Apply a 4-D smoothing filter to estimate $E[S^2]$. Using each measurement in each voxel in turn as a reference, the filter searches within a block of $3 \times 3 \times 3$ neighborhood and across all gradient directions for all measurements that differ from the reference measurement by less than $\sqrt{2}\sigma$. The filtered value is the average of all the measurements that fall within the threshold.
- 3) Estimate the true signal $\hat{S}_R = \sqrt{E[S^2] - 2\sigma^2}$.
- 4) Following [40], obtain the debiased Gaussian-distributed signal \hat{S}_G via $\hat{S}_G = P_G^{-1} \left(P_R(S|\hat{S}_R, \sigma) | \hat{S}_R, \sigma \right)$, where P_G^{-1} is the inverse cumulative distribution function of a Gaussian distribution and P_R is the cumulative probability function of a Rician distribution.

These steps do not involve solving nonlinear problems and are therefore very fast.

III. EXPERIMENTS

A. SMSI Settings

To cover the whole diffusion spectrum, one can set the diffusivity from $0 \text{ mm}^2/\text{s}$ (no diffusion) to $3 \times 10^{-3} \text{ mm}^2/\text{s}$ (free diffusion). However, the portion of the spectrum that is not biologically meaningful can be removed to reduce computational complexity. For the anisotropic compartment, we determined using SMT the range of axial diffusivity based on the body of the corpus callosum. For this purpose, we used adult data from the Human Connectome Project (HCP) [41] and infant data from the Baby Connectome Project (BCP) [42] and found that the effective range for λ_{\parallel} is from $1.5 \times 10^{-3} \text{ mm}^2/\text{s}$ to $2.0 \times 10^{-3} \text{ mm}^2/\text{s}$. Radial diffusivity λ_{\perp} was then set to satisfy $\lambda_{\parallel}/\lambda_{\perp} \geq 1.1$, as in [9]. For the isotropic compartment, we set the diffusivity $\lambda_{\parallel} = \lambda_{\perp}$ from $0 \text{ mm}^2/\text{s}$ to $3 \times 10^{-3} \text{ mm}^2/\text{s}$ with step size $0.1 \times 10^{-3} \text{ mm}^2/\text{s}$. Regularization parameters were automatically selected from the interval of $[10^{-5}, 1]$ as described in Section II-B4.

B. Effects of Orientation Heterogeneity and Isotropic Diffusion

Simulated diffusion data were used to investigate the effects of orientation heterogeneity and free-water diffusion. We used a model consisting of intra-cellular (IC), extra-cellular (EC), and cerebrospinal fluid (CSF) compartments

[7] with normalized signal defined as

$$E = v_{\text{iso}}E_{\text{iso}} + (1 - v_{\text{iso}})(v_{\text{ic}}E_{\text{ic}} + v_{\text{ec}}E_{\text{ec}}), \quad (26)$$

where v_{iso} , v_{ic} , and $v_{\text{ec}} = 1 - v_{\text{ic}}$ are the volume fractions of the isotropic, intra-cellular, and extra-cellular compartments, respectively. E_{iso} , E_{ic} , and E_{ec} are the normalized signals of these compartments. Each compartment was represented by a tensor model: Intra-cellular compartment with $\lambda_{\parallel} = 1.7 \times 10^{-3} \text{ mm}^2/\text{s}$, $\lambda_{\perp} = 0 \text{ mm}^2/\text{s}$; extra-cellular compartment with $\lambda_{\parallel} = 1.7 \times 10^{-3} \text{ mm}^2/\text{s}$, $\lambda_{\perp} = 0.435 \times 10^{-3} \text{ mm}^2/\text{s}$; and the isotropic compartment with $\lambda_{\parallel} = \lambda_{\perp} = 3.0 \times 10^{-3} \text{ mm}^2/\text{s}$. Unless mentioned otherwise, the signal for each shell ($b = 1000, 2000, 3000 \text{ s}/\text{mm}^2$) was generated with 90 non-collinear gradient directions, identical to the HCP protocol [41].

1) *Orientation Heterogeneity*: To demonstrate that SMSI can correctly infer microscopic diffusivity in the presence of orientation heterogeneity, we simulated the signal from micro-environments oriented in 1 to 10 directions distributed equally over a sphere. Rician noise with signal-to-noise ratio (SNR) of 20, typical for HCP and BCP data, were added. We then compared the microscopic diffusion indices computed based on SMSI and DTI. Note that in this experiment, we included only the extra-cellular compartment because it can be sufficiently represented using DTI. Additionally, we also validated SMSI results with simulations including both intra- and extra-cellular compartments, each has volume fraction of 0.5.

2) *Isotropic Diffusion*: Free-water diffusion can confound estimation of microstructure [43], especially in the infant brain typically with high water content [44, 45, 46, 47]. To demonstrate that SMSI can accurately estimate microstructural properties in the presence of isotropic diffusion, we simulated the signal with intra-cellular, extra-cellular, and isotropic compartments with $v_{\text{ic}} = v_{\text{ec}} = 0.5$ and v_{iso} ranging from 0 to 0.9 in steps of 0.1. Rician noise with SNR of 20 was added. We validated the effectiveness of SMSI via microscopic FA and MD as well as extra-cellular, intra-cellular, and isotropic volume fractions. SMSI was compared with SMT [12], multi-compartment SMT (MC-SMT) [13], and NODDI [8].

C. Microscopic Anisotropy and Orientation Coherence

We compared the MAI and OCI values given by SMSI, SMT, MC-SMT, and NODDI. MAI[†] was used for both SMSI and NODDI since both models account for the isotropic volume fraction. MAI was used for SMT and MC-SMT. MAI and MAI[†] were validated with respect to different isotropic volume fractions. OCI is intrinsically robust to isotropic diffusion and is computed for micro-environments with increasing number of directions.

D. Number of *b*-Shells

We evaluated the minimal number of *b*-shells needed for effective SMSI estimation. We used a 21-shell data of a healthy adult with *b*-values ranging from 500 s/mm² to 3000 s/mm² with step size 125 s/mm², acquired with non-collinear gradients, i.e., 4 diffusion-weighted (DW) images for $b = 500 \text{ s}/\text{mm}^2$, 5 for $b = 625 \text{ s}/\text{mm}^2$, ..., 23 for $b = 2875 \text{ s}/\text{mm}^2$, and 24 for $b = 3000 \text{ s}/\text{mm}^2$, in addition to 13 non-DW images, resulting in a total of 307 volumes. The images were acquired with an 140 × 140 imaging matrix, 1.5 mm × 1.5 mm × 1.5 mm resolution, TE=89 ms, TR=2513 ms, and multi-band factor 5. We applied SMSI to

- 1) The 21-shell dataset consisting of all images;
- 2) The 11-shell dataset with b -values from 500 s/mm^2 to 3000 s/mm^2 with step size 250 s/mm^2 ;
- 3) The 6-shell dataset with b -values from 500 s/mm^2 to 3000 s/mm^2 with step size 500 s/mm^2 ;
- 4) The 3-shell-1000 with b -values from 1000 s/mm^2 to 3000 s/mm^2 with step size 1000 s/mm^2 ; and
- 5) The 3-shell-500 dataset with b -values from 500 s/mm^2 to 2500 s/mm^2 with step size 1000 s/mm^2 .

The different sampling schemes were compared with the 21-shell dataset as the reference.

E. Longitudinal Infant Data

To demonstrate the effectiveness of SMSI in probing microstructural changes in the early developing human brain, we used the longitudinal datasets of two infants from the Baby Connectome Project (BCP) [42]. The first subject was scanned at 54, 146, and 223 days after birth and the second subject were scanned at 318, 410, and 514 days after birth. The diffusion data were acquired using a Siemens 3T Magnetom Prisma MRI scanner with the following protocol: 140×140 imaging matrix, $1.5 \text{ mm} \times 1.5 \text{ mm} \times 1.5 \text{ mm}$ resolution, $TE=88 \text{ ms}$, $TR=2365 \text{ ms}$, 32-channel receiver coil, and multi-band factor 5. DW images for 9, 12, 17, 24, 34, and 48 non-collinear gradient directions were collected respectively for $b = 500, 1000, 1500, 2000, 2500, 3000 \text{ s/mm}^2$. A non-DW image $b = 0 \text{ s/mm}^2$ was collected for every 24 images, giving a total of 6. Image reconstruction was performed using SENSE1 [48], resulting in non-stationary Rician noise distribution. The magnitude signal was debiased as described in Section II-B5. Diffusion indices were compared between SMSI, SMT, MC-SMT, and NODDI.

IV. RESULTS

A. Orientation Heterogeneity

From Fig. 5 (a) and (b), one can appreciate that DTI FA and MD decrease with the number of orientations whereas SMSI μFA and μMD remain consistent. Similarly, Fig. 5 (c) and (d) confirm the robustness of SMSI to orientation heterogeneity in case of multiple compartments. Fig. 6 shows FA (top left) and μFA (top right) of a representative HCP subject. DTI FA results in a dark band due to lower anisotropy caused by fiber crossings. SMSI μFA reveals the true anisotropy unconfounded by fiber dispersion. SMSI OCI quantifies orientation dispersion. A close-up view of a region with three-way crossings as shown by the fiber orientation distribution functions (ODFs) confirms this observation.

B. Isotropic Diffusion

1) *Microscopic FA and MD*: Fig. 5 (e) and (f) show the microstructural properties estimated using SMT and SMSI. The SMT model is a single-compartment model and does not account for isotropic diffusion. Hence, SMT μFA and μMD are significantly affected by the isotropic volume fraction. Note that even when the isotropic volume fraction is low, the results given by SMT, unlike SMSI, deviate from the ground truth. SMSI μFA^\dagger and μMD^\dagger are robust to isotropic diffusion.

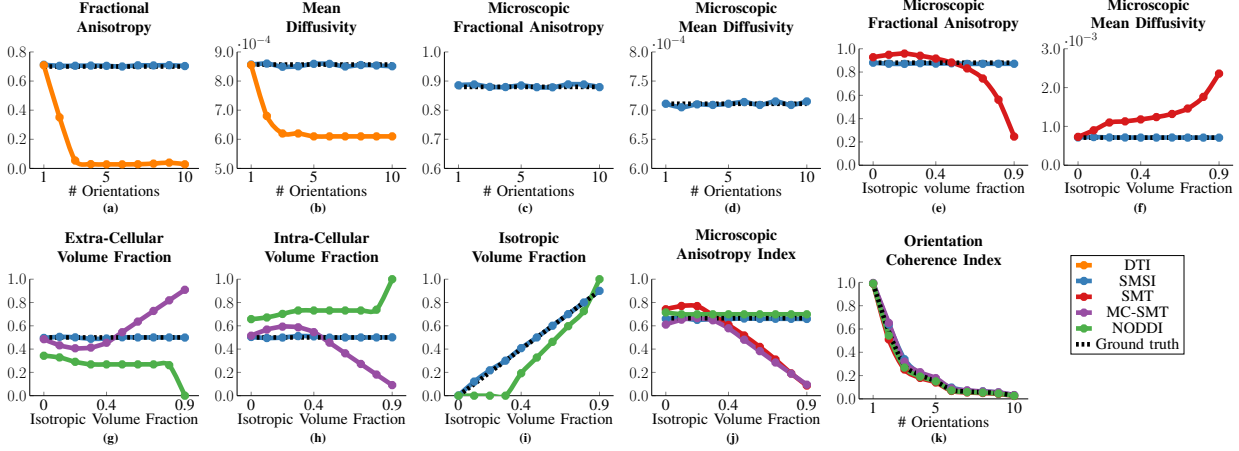


Fig. 5. **Numerical Validations.** Comparison of SMSI with DTI, SMT, MC-SMT, and NODDI. (a) and (b): DTI FA and MD and SMSI μ FA and μ MD with respect to the number of crossing fibers. (c) and (d): SMSI μ FA and μ MD with respect to orientation heterogeneity (with multiple compartments). (e) and (f): SMT μ FA and μ MD and SMSI μ FA † and μ MD † with respect to isotropic volume fraction. (g) and (h): Estimates of v_{ec} and v_{ic} given by SMSI, MC-SMT, and NODDI with respect to isotropic volume fraction. (i): Estimates of v_{iso} given by SMSI and NODDI with respect to isotropic volume fraction. (j) and (k): Microscopic anisotropy index (MAI) with respect to isotropic volume fraction and orientation coherence index (OCI) with respect to the number of orientations given by SMSI, SMT, MC-SMT, and NODDI. MAI † was calculated for SMSI and NODDI. Values shown are the means of 1000 repetitions. Standard deviations are negligible and hence not displayed.

2) *Extra- and Intra-Cellular Volume Fractions:* Fig. 5 (g) and (h) show that NODDI underestimates the extra-cellular volume fraction and overestimates the intra-cellular volume fraction for all isotropic volume fractions. The bias is due to the fixed intrinsic parallel diffusivity assumption in the NODDI implementation [49]. MC-SMT produces correct estimates when the isotropic volume fraction is 0. However, when isotropic volume fraction increases, MC-SMT fails to yield accurate results as it does not account for isotropic diffusion and its tortuosity assumption on the extra-cellular radial diffusivity [13]. SMSI gives correct and consistent results. Notice that estimation bias occurs even when the isotropic volume fraction is small. We will show that for in vivo data MC-SMT and NODDI exhibit similar bias in underestimating the extra-cellular volume fraction and overestimating the intra-cellular volume fraction.

3) *Isotropic Diffusion Estimation:* Fig. 5 (i) shows that SMSI yields accurate estimates of the isotropic volume fraction, which NODDI however tends to underestimate, especially when the actual value is less than 0.3.

C. Microscopic Anisotropy and Orientation Coherence

Fig. 5 (j) shows the MAI values given by SMSI, SMT, MC-SMT, and NODDI. MAI † was computed for SMSI and NODDI since they explicitly considers isotropic diffusion. Similar to the trend of μ FA, SMT overestimates/underestimates MAI when the isotropic volume fraction is low/high. MC-SMT exhibits a similar trend but the bias is smaller thanks to the two-compartment model. NODDI is more stable but introduces a systematic bias across isotropic volume fractions. SMSI yields results that are close to the ground truth. Fig. 5 (k) shows that all methods produce OCI values that are close to the ground truth and decrease with increasing number of orientations.

Fig. 7 shows similar trends for in vivo data. In white matter where isotropic volume fraction is low, SMT and MC-SMT yield significantly higher MAI values than SMSI and NODDI. The MAI † values given by SMSI and

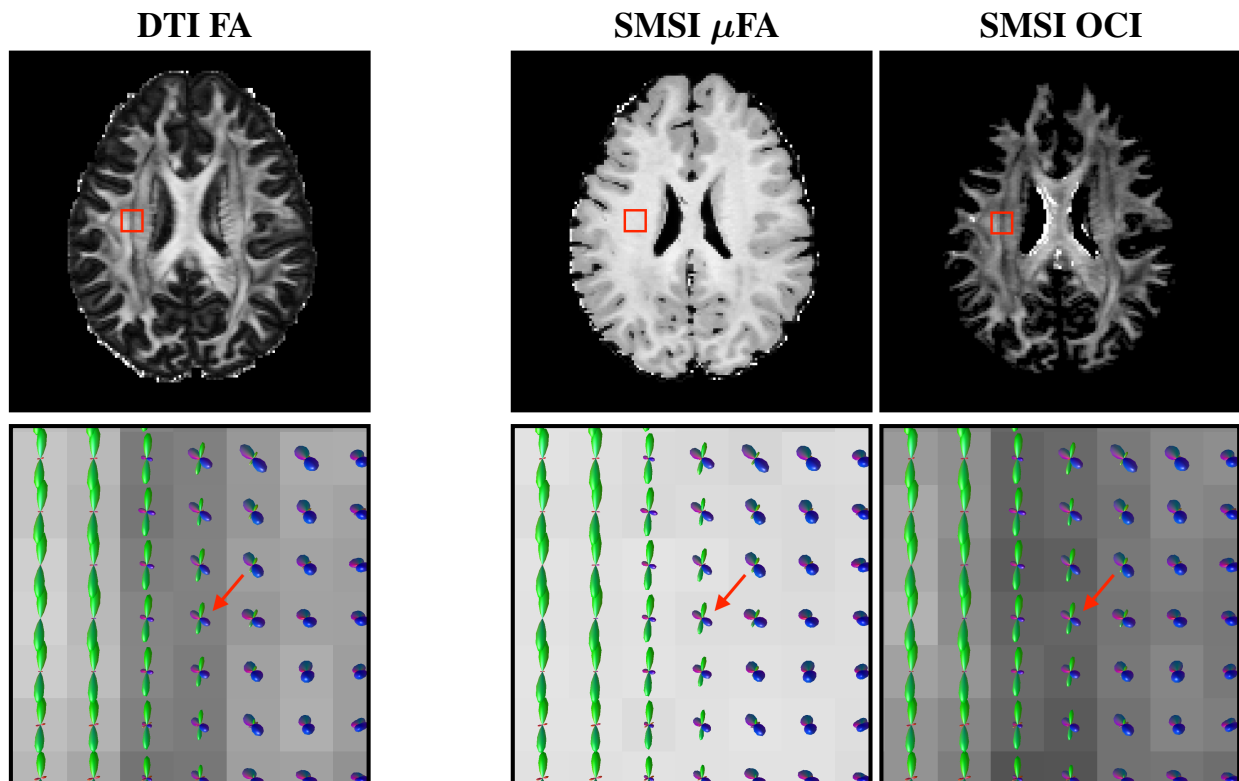


Fig. 6. **Voxel and Microscopic FA.** Top: DTI FA, SMSI μ FA, and SMSI OCI. Bottom: Close-up view with fiber ODF overlaid. Red arrows mark the region with crossing fibers.

NODDI in superficial white matter are higher as both methods eliminate the isotropic diffusion contamination. NODDI returns slightly higher MAI[†] than SMSI. OCI values, on the other hand, are almost similar for all methods, with SMT giving slightly lower values. All these observations are consistent with Fig. 5 (j) and (k).

D. Diffusion Indices

Fig. 8 shows that SMSI provides a wider range of diffusion indices than SMT, MC-SMT, and NODDI, allowing greater specificity in characterizing tissue microstructure. The discrepancies between SMSI and the other methods can be explained based on our previous observations from the synthetic data experiments. For instance, one can observe that μ FA given by SMT is higher than SMSI in gray matter. This is consistent with our previous observation that SMT overestimates μ FA when the actual value is low (Fig. 5 (e) and (f)). MC-SMT overestimates and NODDI underestimates the extra-cellular volume fraction when its actual value is high (Fig. 5 (g) and (h)), such as in gray matter. Additionally, NODDI yields higher isotropic volume fraction in deep white matter than gray matter (Fig. 5 (i)), which does not reflect the fact that isotropic diffusion should be less prominent in deep white matter in view of the tightly packed micro-architecture, particularly in the adult brain [50, 51]. On the other hand, SMSI gives more biologically feasible results with lower isotropic volume fraction in white matter than gray matter. Note that isotropic diffusion in gray matter is in part intra-soma diffusion [52, 53].

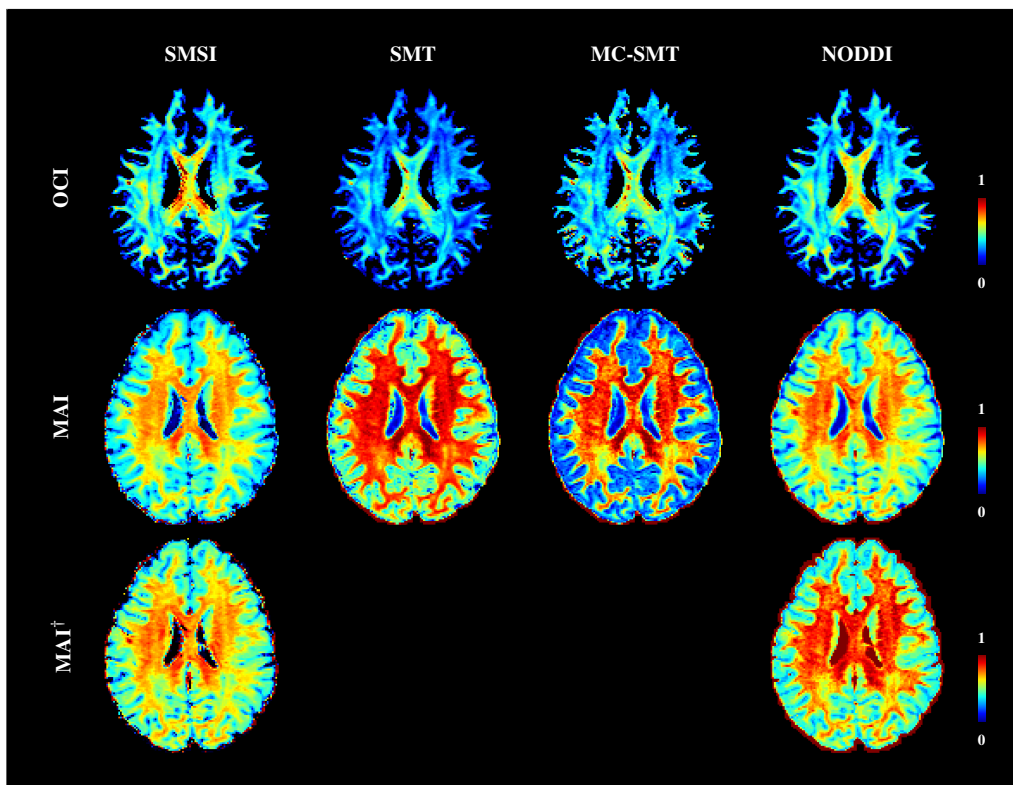


Fig. 7. **Microscopic Anisotropy and Orientation Coherence.** Microscopic anisotropy (MAI) and orientation coherence index (OCI) maps given by SMSI, SMT, MC-SMT, and NODDI. MAI[†] is computed only for SMSI and NODDI. A subject from the HCP was used.

E. Number of b -Shells

Fig. 9 shows the scatter plots and histograms of representative SMSI indices of different sampling schemes with ‘21-shell’ as the reference. The 11-shell sampling scheme produces results closest to the reference as shown by the high histogram similarity and the high correlation coefficient. Fewer number of shells still yield reasonable results with correlation coefficient $R > 0.9$. The 3-shell-500 scheme is better than 3-shell-1000 in estimating the isotropic volume fraction thanks to the $b = 500 \text{ s/mm}^2$ shell as the signal of free water decays significantly at $b = 1000 \text{ s/mm}^2$. SMSI is hence applicable to many public datasets, such as the HCP (3 shells) and the BCP (6 shells) datasets.

F. Longitudinal Infant Data

Fig. 10 shows longitudinal microstructural changes quantified via SMSI indices. Note that IDE anisotropy indices (third and fourth columns) give higher values than non-IDE indices (first and second columns) since isotropic diffusion lowers anisotropy.

With brain development, anisotropy, coherence, and intra-cellular volume fraction increase and isotropic and extra-cellular volume fraction decrease. Spatially, development progresses from center to peripheral, and from posterior to anterior. This is line with prior knowledge about myelination and axon maturation [29].

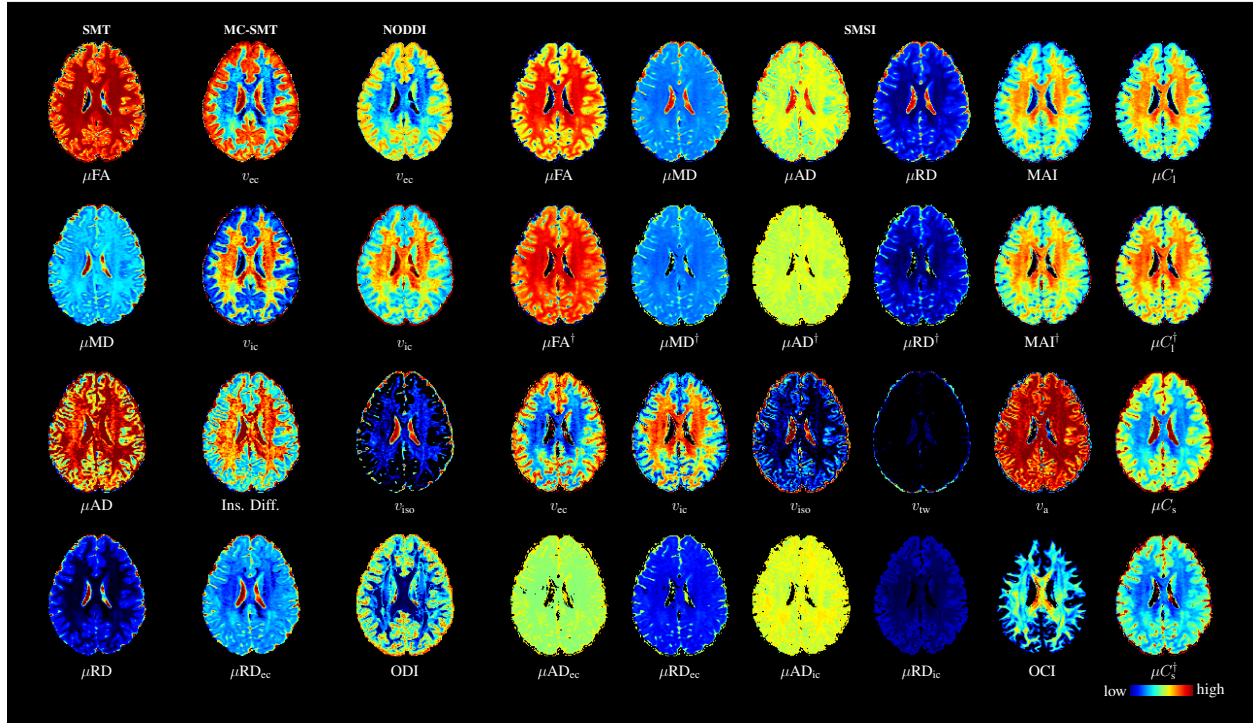


Fig. 8. **Diffusion Indices.** Diffusion indices of SMSI, SMT, MC-SMT, and NODDI. The intrinsic diffusivity (Ins. Diff.) of MC-SMT is the longitudinal diffusivity common for both extra- and intra-cellular compartments. Jet color mapping, with cool colors for low values and warm colors for high values, is used. The values range from 0 to 0.003 for diffusivity-based indices and 0 to 1 for other indices. Please refer to Table I for the definitions of the indices.

Fig. 11 presents results given by SMT, MC-SMT, and NODDI. Comparing with Fig. 10, a noteworthy difference is NODDI significantly underestimates the isotropic volume fraction (Fig. 5 (i)), giving zero values in most of gray matter across all time points. This is contradictory to the observation that infant brains typically have higher water content during early development, which decreases later during brain maturation [44, 45] due to a combination of multiple factors such as natural water reduction in the body [46], the growth of neuronal and glial cells [47], and myelination [54, 55]. Note also that MC-SMT and NODDI give higher intra-cellular fraction and lower extra-cellular volume fraction (Fig. 5 (g) and (h)). SMT overestimates μFA (Fig. 5 (e) and (f)) especially in deep white matter regions. For example, at the splenium of the corpus callosum, the values are almost always maximum, i.e., 1, across all time points. This observation contradicts with previous findings that these regions are immature at birth and undergo a progressive development during infancy [56, 57].

V. DISCUSSION

Heterogeneously oriented micro-environments are ubiquitous in brain tissues. We have introduced SMSI as a flexible tool for quantification of microarchitecture, unconfounded by orientation heterogeneity. Unlike SMT, MC-SMT, and NODDI, SMSI does not rely on a model that is based on a predefined number of compartments. SMSI allows the data to speak for themselves via diffusion characterization using the spherical mean spectrum. We have

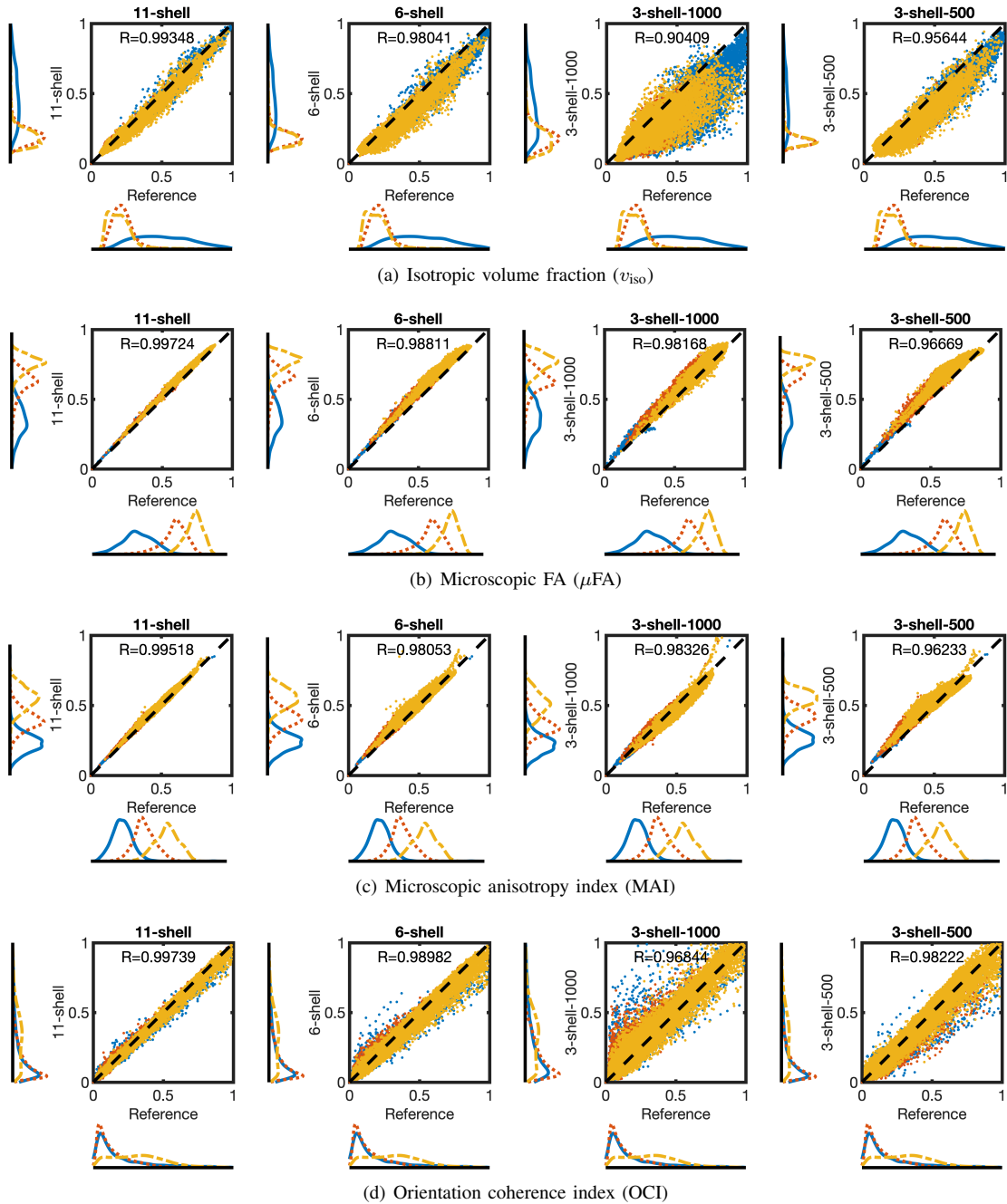


Fig. 9. **Number of b-Shells.** Scatter plots and histograms of representative SMSI scalars indices of sampling schemes 11-shell, 6-shell, 3-shell-1000, and 3-shell-500 with 21-shell as the reference. Voxels are classified as CSF (blue), gray matter (red), or white matter (yellow). For better visibility, only one in every six voxels is shown.

shown that proper modeling of isotropic diffusion is of paramount importance for accurate characterization of microstructural properties. Failure to do so significantly biases microstructural estimates.

In addition to the infant brain, SMSI, owing to its ability in characterizing the whole diffusion spectrum, can be employed to quantify adult brain changes and pathologies, such as increased cellularity and vasogenic oedema associated with inflammatory demyelination and axonal injury common in multiple sclerosis [16]. SMSI can also

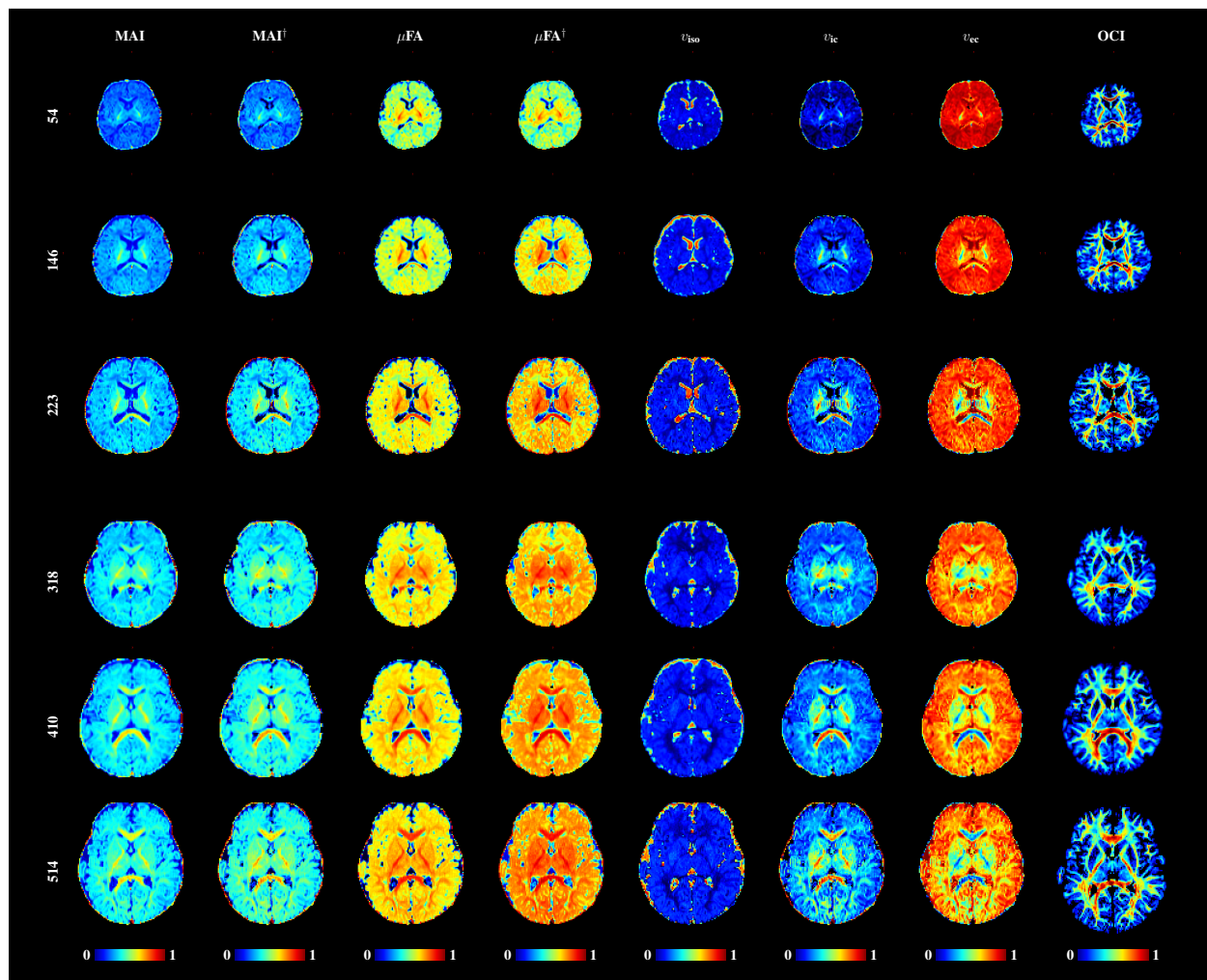


Fig. 10. **Longitudinal Development of Microstructure.** Microstructural development of two BCP subjects: one scanned at 54, 146, and 223 days after birth (top panel) and the other at 318, 410, and 514 days after birth (bottom panel).

be applied to organs beyond the brain.

Microstructural estimation has been reported to be affected by degeneracy caused by (i) the interplay of orientation dispersion and diffusion anisotropy [58, 59], and (ii) the inability of the spherical mean in distinguishing some cases of anisotropic diffusion from isotropic diffusion [38, 60]. In the first type of degeneracy, a set of orientation coherent low-anisotropy tensors could result in the same diffusion signal as a set of dispersed high-anisotropy tensors. This degeneracy can be resolved by using the spherical mean due to its invariance to the orientation distribution [12]. In the second type of degeneracy, the spherical mean signal of an anisotropic tensor can be indistinguishable from that of a combination of multiple isotropic tensors with different diffusivity [38]. This degeneracy can be mitigated by additional data acquired for example via spherical tensor encoding (STE) [60, 61]. STE can be used in combination with linear tensor encoding (LTE) to provide a means to measure microscopic anisotropy independent of the orientation distribution [58]. While effective, STE data are not commonly available. We discuss next how SMSI, which utilizes the full direction-sensitive signal in addition to the spherical mean signal (see Section II-B4),

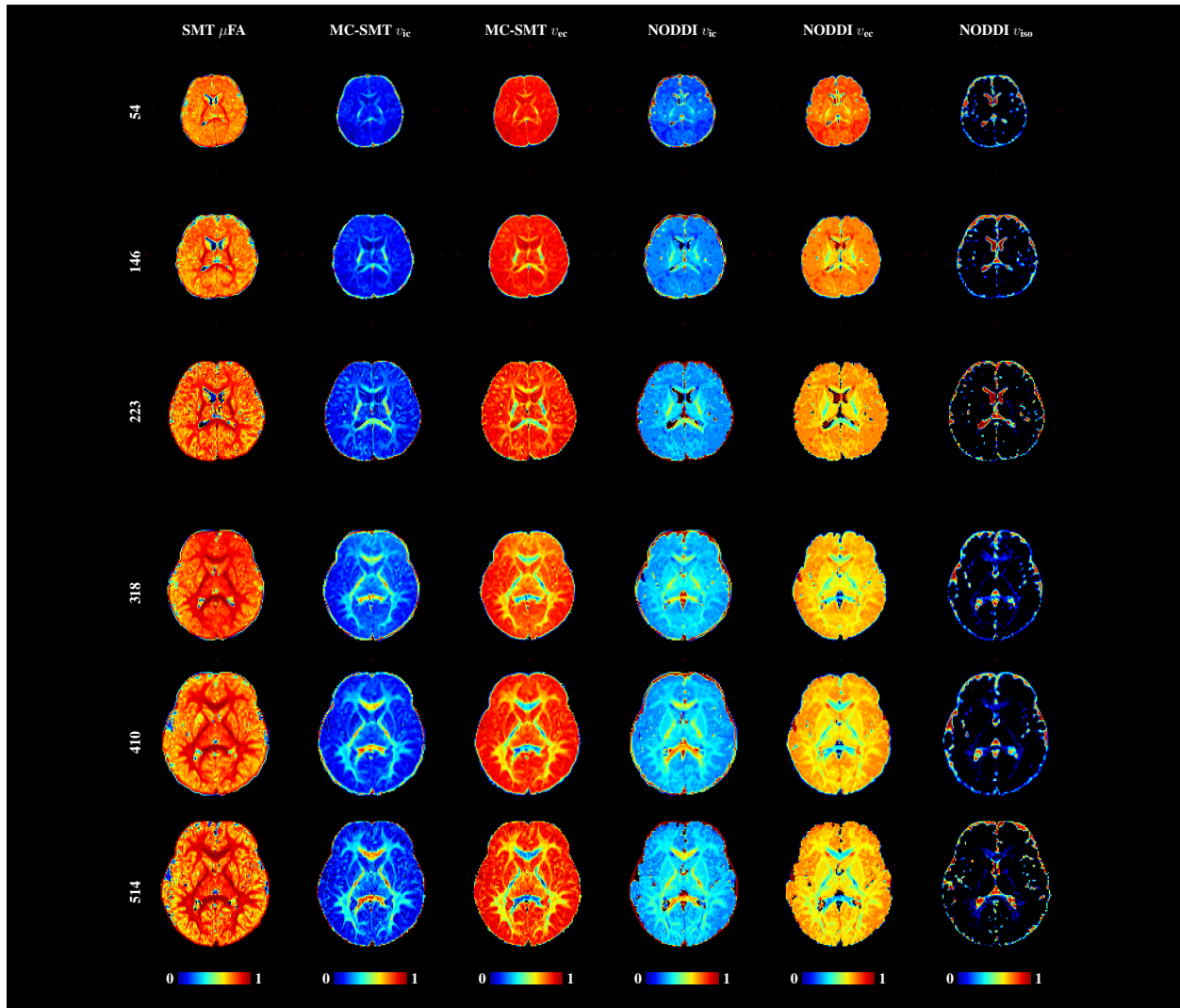


Fig. 11. **Longitudinal SMT, MC-SMT, and NODDI Indices.** Similar to Fig. 10 but based on SMT, MC-SMT, and NODDI.

can be used to resolve this degeneracy. The full signal, unlike the mean signal, is not ambiguous in distinguishing isotropic and anisotropic diffusion.

Ideally, different combinations of diffusion compartments are expected to give different mean signals. However, in practice, the difference between the mean signals of an anisotropic diffusion compartment and a combination of multiple isotropic diffusion compartments at different scales might be negligibly small [38].

To illustrate the degeneracy problem, we simulated DW signals from different configurations:

- 1) Case 0: Zeppelins with $AD = 1.7 \mu\text{m}^2/\text{ms}$ and $RD = 0.4 \mu\text{m}^2/\text{ms}$.
- 2) Case 1: Isotropic diffusion at two different scales with $AD = RD = 0.5 \mu\text{m}^2/\text{ms}$ and $AD = RD = 1.1 \mu\text{m}^2/\text{ms}$ with equal volume fractions.
- 3) Case 2: Same as Case 1 but with $AD = RD = 0.7 \mu\text{m}^2/\text{ms}$ and $AD = RD = 1.0 \mu\text{m}^2/\text{ms}$.
- 4) Case 3: Same as Case 1 but with $AD = RD = 0.3 \mu\text{m}^2/\text{ms}$ and $AD = RD = 1.3 \mu\text{m}^2/\text{ms}$.

5) Case 4: Same as Case 1 but with $AD = RD = 0.3 \mu\text{m}^2/\text{ms}$ and $AD = RD = 1.1 \mu\text{m}^2/\text{ms}$.

Fig. 12 illustrates the cases and their respective spherical mean signals. The signal of Case 1 is almost identical to Case 0, causing degeneracy. The signals of the other cases differ from Case 0, but the small differences can still cause degeneracy, especially when the SNR is low. We also tested our method on mixtures of Case 0 and Case 1 with varying volume fractions.

As described in Section II-B4, multi-scale isotropic diffusion may degenerate anisotropic fODFs to isotropic fODFs. Hence, a good way to identify this FSS degeneracy is to gauge the isotropy of each anisotropic fODF, which can be measured with the help of generalized fractional anisotropy (GFA) [39]:

$$ISO = \sqrt{1 - \text{GFA}^2}. \quad (27)$$

Anisotropic atoms with $ISO \geq 0.95$ ($\text{GFA} < 0.3$) are considered degenerate. This is captured by an indicator function for the i -th atom:

$$\Upsilon[i] = \begin{cases} 1, & \text{ISO}[i] \geq 0.95, \\ 0, & \text{otherwise.} \end{cases} \quad (28)$$

Note that even if an atom is affected by degeneracy, the effect on microstructural estimation might be minimal if the volume fraction associated with the atom is small. We assess the severity of degeneracy via a degeneracy index (DI):

$$DI = \sum_i \nu[i] \Upsilon[i], \quad (29)$$

which is a linear combination of the elements in Υ weighted by the corresponding volume fractions ν of the anisotropic atoms. DI ranges from 0 to 1, with higher values indicating greater degeneracy. If either isotropy or volume fraction is low, the DI is low and the effect of degeneracy is negligible.

Our implementation of SMSI breaks the degeneracy by utilizing complementary information from the full diffusion signal and the spherical mean signal. This full signal captures directional information and can hence distinguish between isotropic and anisotropic diffusion even if the spherical mean signals of the two cases are identical. Fig. 13 indicates that the full signal alone is unable to fully resolve the degeneracy, yielding high DI (Fig. 13(a)) and inaccurate volume fraction estimates (Fig. 13(c)). Case 1 has the highest DI since, instead of isotropic tensors, it can be represented equally with degenerate anisotropic tensors. SMSI suppresses the degenerate atoms and lowers the DI (Fig. 13(b)), resulting in accurate volume fraction estimates (Fig. 13(d)). Fig. 13(e) shows the results for different mixtures of Case 0 and Case 1.

Figure 14 shows the DI maps given by the FSS on a HCP dMRI dataset [41]. Less than 1% of the total brain voxels, mostly beyond the brain parenchyma, are affected by degeneracy, implying that the problem is not severe in practice, at least for the healthy adult brain. Degeneracy suppression with SMSI results in less than 0.1% voxels with non-zero DI values. The DI statistics for 20 HCP subjects are summarized in Table II.

Similar to AMICO [8], SMSI estimation can be potentially improved via deep learning, as demonstrated by Microstructure Estimation using a Deep Network (MEDN) [62]. This will allow the estimation of tissue

TABLE II
DEGENERACY INDEX STATISTICS FOR 20 HCP SUBJECTS.

	FSS Only	SMSI
% non-zero DI voxels	0.813	0.056
DI range	0.001 - 0.712	0.002 - 0.558
DI mean	0.073	0.017
DI standard deviation	0.101	0.072

microstructure properties using of clinical dMRI acquired with a limited number of diffusion gradients.

SMSI involves convex and fast numerical optimization. Based on our preliminary MATLAB implementation, running SMSI on an 1.5 mm isotropic resolution infant dataset for the whole brain on a 4.2GHz Core i7 machine typically takes 15 minutes. Implementation with C++ will likely further significantly improve the speed. SMSI is therefore well suited for large-scale studies.

VI. CONCLUSION

We have presented in this paper a flexible method for quantification of microarchitecture, called spherical mean spectrum imaging (SMSI). The SMS encodes the volume fractions associated with a spectrum of diffusion scales. This allows a wide variety of features to be computed for comprehensive microstructural analysis. We have demonstrated the utility of SMSI in probing the tissue microarchitecture of the developing brain. We have in fact demonstrated that SMSI shows greater sensitivity to brain development [63] and reveals distinct developmental patterns of cortical microstructure [64]. Future work entails applying SMSI to investigating brain pathologies and potentially identifying sensitive and specific biomarkers for disease diagnosis.

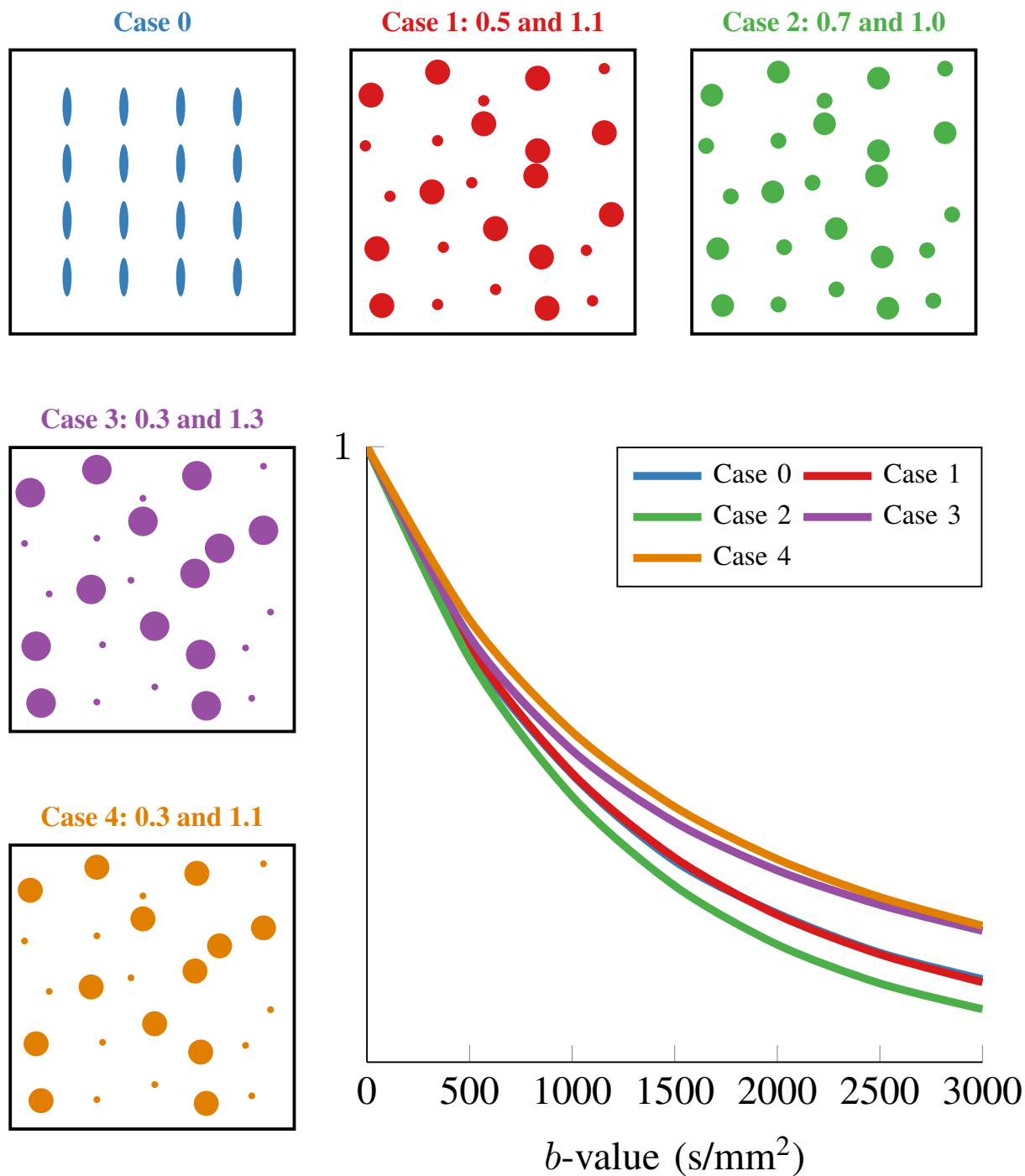


Fig. 12. **Degeneracy.** Spherical mean signals of anisotropic (Case 0) and isotropic (Cases 1–4) configurations. Case 1 has spherical mean signal almost identical to Case 0.

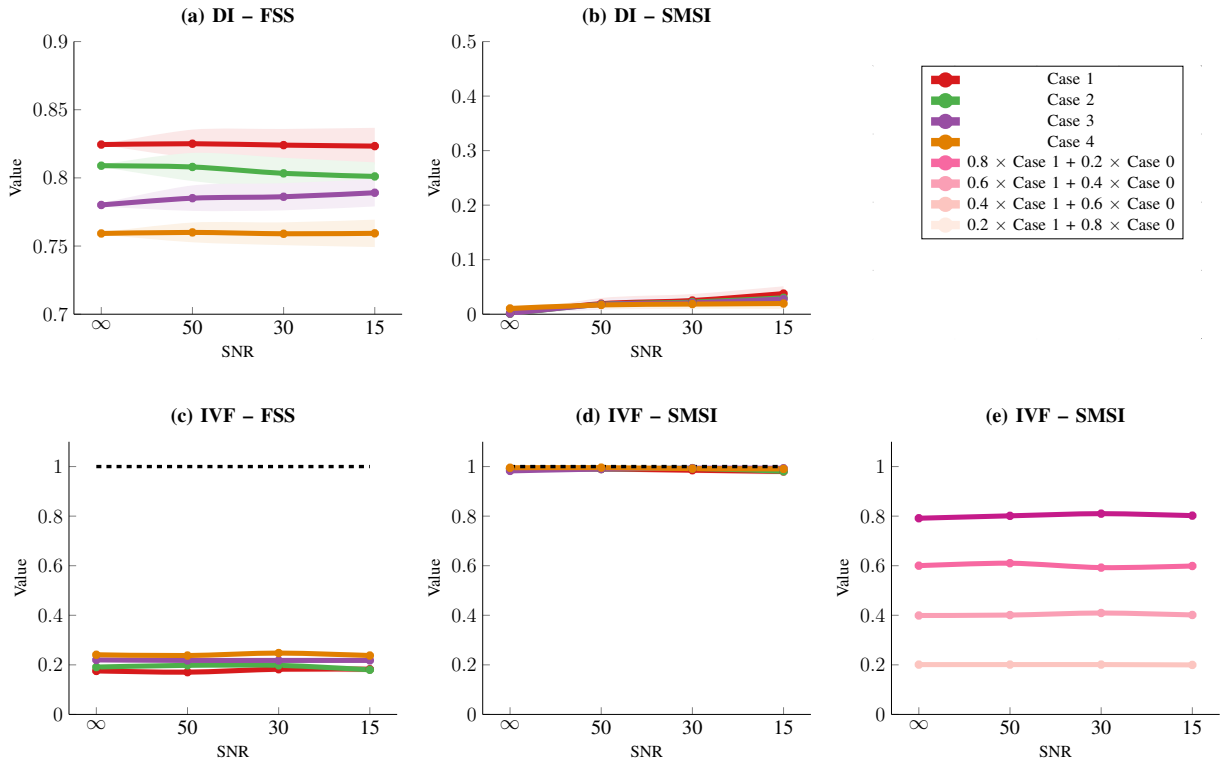


Fig. 13. **Degeneracy.** DI values and IVF estimates given by FSS and SMSI for the different configurations in Fig. 12 and different combinations of Case 0 and Case 1. The dashed lines represent the ground truth. Shaded regions represent standard deviations computed based on 1000 instances for each SNR. The DI of Case 0 is 0 and is hence not shown. The standard deviations of the IVFs are negligible.

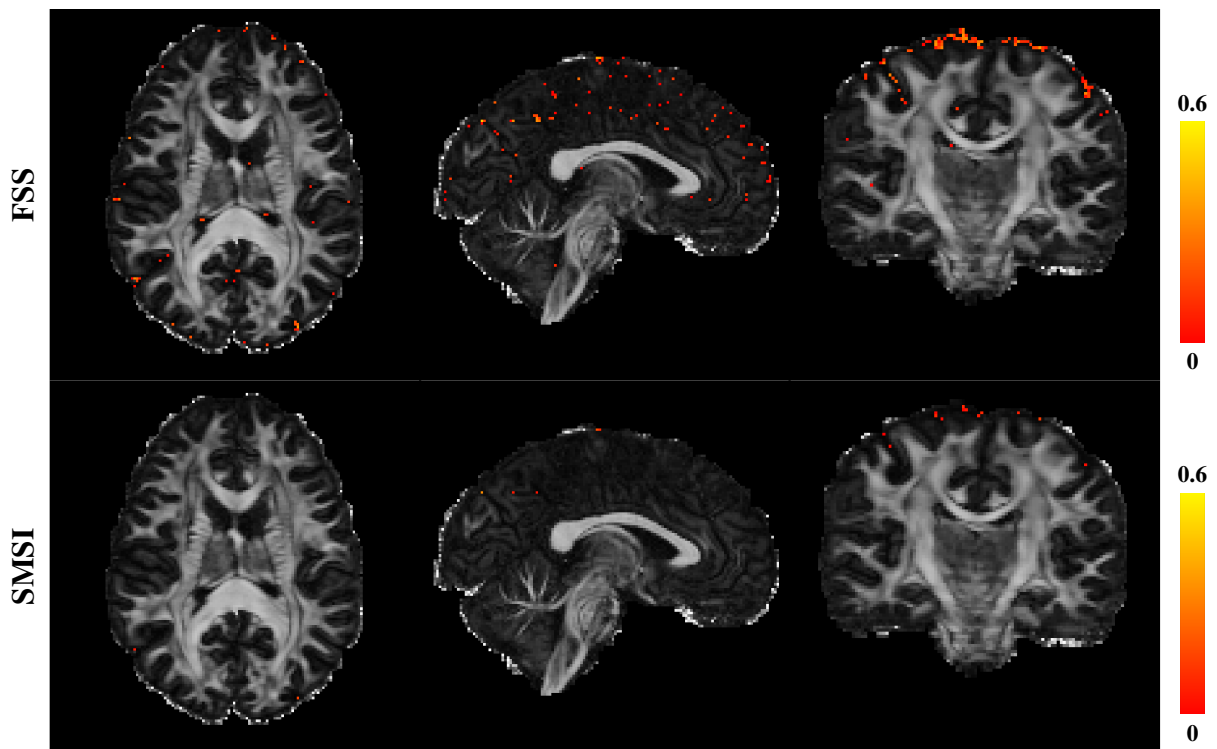


Fig. 14. **Degeneracy Index.** DI maps, overlaid on FA images, given by FSS only and SMSI for a representative HCP subject.

REFERENCES

- [1] N. Kunz, H. Zhang, L. Vasung, K. R. O'Brien, Y. Assaf, F. Lazeyras, D. C. Alexander, and P. S. Hüppi, "Assessing white matter microstructure of the newborn with multi-shell diffusion MRI and biophysical compartment models." *NeuroImage*, vol. 96, no. 8, pp. 288–299, 2014.
- [2] B. Lampinen, F. Szczepankiewicz, J. Mårtensson, D. van Westen, P. C. Sundgren, and M. Nilsson, "Neurite density imaging versus imaging of microscopic anisotropy in diffusion MRI: A model comparison using spherical tensor encoding." *NeuroImage*, vol. 147, pp. 517–531, 2017.
- [3] Y. Assaf and P. J. Basser, "Composite hindered and restricted model of diffusion (CHARMED) MR imaging of the human brain," *NeuroImage*, vol. 27, no. 1, pp. 48–58, 2005.
- [4] Y. Assaf, T. Blumenfeld-Katzir, Y. Yovel, and P. J. Basser, "AxCaliber: A method for measuring axon diameter distribution from diffusion MRI," *Magnetic Resonance in Medicine*, vol. 59, no. 6, pp. 1347–1354, 2008.
- [5] D. C. Alexander, P. L. Hubbard, M. G. Hall, E. A. Moore, M. Ptito, G. J. Parker, and T. B. Dyrby, "Orientationally invariant indices of axon diameter and density from diffusion MRI," *NeuroImage*, vol. 52, no. 4, pp. 1374–1389, 2010.
- [6] E. Fieremans, J. H. Jensen, and J. A. Helpert, "White matter characterization with diffusional kurtosis imaging," *NeuroImage*, vol. 58, no. 1, pp. 177–188, 2011.
- [7] H. Zhang, T. Schneider, C. A. Wheeler-Kingshott, and D. C. Alexander, "NODDI: Practical in vivo neurite orientation dispersion and density imaging of the human brain," *NeuroImage*, vol. 61, no. 4, pp. 1000–1016, 2012.
- [8] A. Daducci, E. J. Canales-Rodríguez, H. Zhang, T. B. Dyrby, D. C. Alexander, and J.-P. Thiran, "Accelerated microstructure imaging via convex optimization (AMICO) from diffusion MRI data," *NeuroImage*, vol. 105, pp. 32–44, 2015.
- [9] N. S. White, T. B. Leergaard, H. D'arceuil, J. G. Bjaalie, and A. M. Dale, "Probing tissue microstructure with restriction spectrum imaging: Histological and theoretical validation," *Human Brain Mapping*, vol. 34, no. 2, pp. 327–346, 2013.
- [10] J.-D. Tournier, F. Calamante, D. G. Gadian, and A. Connelly, "Direct estimation of the fiber orientation density function from diffusion-weighted MRI data using spherical deconvolution," *NeuroImage*, vol. 23, no. 3, pp. 1176–1185, 2004.
- [11] J.-D. Tournier, F. Calamante, and A. Connelly, "Robust determination of the fibre orientation distribution in diffusion MRI: Non-negativity constrained super-resolved spherical deconvolution," *NeuroImage*, vol. 35, pp. 1459–1472, 2007.
- [12] E. Kaden, F. Kruggel, and D. C. Alexander, "Quantitative mapping of the per-axon diffusion coefficients in brain white matter," *Magnetic Resonance in Medicine*, vol. 75, no. 4, pp. 1752–1763, 2016.
- [13] E. Kaden, N. D. Kelm, R. P. Carson, M. D. Does, and D. C. Alexander, "Multi-compartment microscopic diffusion imaging," *NeuroImage*, vol. 139, pp. 346–359, 2016.
- [14] B. Scherrer, A. Schwartzman, M. Taquet, M. Sahin, S. P. Prabhu, and S. K. Warfield, "Characterizing brain tissue by assessment of the distribution of anisotropic microstructural environments in diffusion-compartment imaging (DIAMOND)," *Magnetic Resonance in Medicine*, vol. 76, no. 3, pp. 963–977, 2016.
- [15] D. Yablonskiy, G. Bretthorst, and J. Ackerman, "Statistical model for diffusion attenuated MR signal," *Magnetic Resonance in Medicine*, vol. 50, pp. 664–669, 2003.
- [16] Y. Wang, Q. Wang, J. P. Haldar, F.-C. Yeh, M. Xie, P. Sun, T.-W. Tu, K. Trinkaus, R. S. Klein, A. H. Cross, and S.-K. Song, "Quantification of increased cellularity during inflammatory demyelination," *Brain*, vol. 134, pp. 3590–3601, 2011.
- [17] T. Paus, D. Collins, A. Evans, G. Leonard, B. Pike, and A. Zijdenbos, "Maturation of white matter in the human brain: a review of magnetic resonance studies," *Brain Research Bulletin*, vol. 54, no. 3, pp. 255–266, 2001.
- [18] S. C. Partridge, P. Mukherjee, R. G. Henry, S. P. Miller, J. I. Berman, H. Jin, Y. Lu, O. A. Glenn, D. M. Ferriero, A. J. Barkovich, and B. V. Daniel, "Diffusion tensor imaging: serial quantitation of white matter tract maturity in premature newborns," *NeuroImage*, vol. 22, no. 3, pp. 1302–1314, 2004.
- [19] J. Dubois, L. Hertz-Pannier, G. Dehaene-Lambertz, Y. Cointepas, and D. Le Bihan, "Assessment of the early organization and maturation of infants' cerebral white matter fiber bundles: a feasibility study using quantitative diffusion tensor imaging and tractography," *NeuroImage*, vol. 30, no. 4, pp. 1121–1132, 2006.
- [20] M. Anjari, L. Srinivasan, J. M. Allsop, J. V. Hajnal, M. A. Rutherford, A. D. Edwards, and S. J. Counsell, "Diffusion tensor imaging with tract-based spatial statistics reveals local white matter abnormalities in preterm infants," *NeuroImage*, vol. 35, no. 3, pp. 1021–1027, 2007.
- [21] K. J. Kersbergen, A. Leemans, F. Groenendaal, N. E. van der Aa, M. A. Viergever, L. S. de Vries, and M. J. Benders, "Microstructural brain development between 30 and 40 weeks corrected age in a longitudinal cohort of extremely preterm infants," *NeuroImage*, vol. 103, pp. 214–224, 2014.
- [22] J. Rose, R. Vassar, K. Cahill-Rowley, X. S. Guzman, D. K. Stevenson, and N. Barnea-Goraly, "Brain microstructural development at near-term age in very-low-birth-weight preterm infants: An atlas-based diffusion imaging study," *NeuroImage*, vol. 86, pp. 244–256, 2014.
- [23] J. Dubois, G. Dehaene-Lambertz, M. Perrin, J.-F. Mangin, Y. Cointepas, E. Duchesnay, D. Le Bihan, and L. Hertz-Pannier, "Asynchrony of the early maturation of white matter bundles in healthy infants: Quantitative landmarks revealed noninvasively by diffusion tensor imaging," *Human Brain Mapping*, vol. 29, no. 1, pp. 14–27, 2008.
- [24] E. V. Sullivan and A. Pfefferbaum, "Diffusion tensor imaging and aging," *Neuroscience & Biobehavioral Reviews*, vol. 30, no. 6, pp. 749–761, 2006.
- [25] I. O. Jelescu, J. Veraart, V. Adisetiyo, S. S. Milla, D. S. Novikov, and E. Fieremans, "One diffusion acquisition and different white matter models: How does microstructure change in human early development based on WMTI and NODDI?" *NeuroImage*, vol. 107, pp. 242–256, 2015.
- [26] D. C. Dean, J. O'muircheartaigh, H. Dirks, B. G. Travers, N. Adluru, A. L. Alexander, and S. C. Deoni, "Mapping an index of the myelin g-ratio in infants using magnetic resonance imaging," *NeuroImage*, vol. 132, pp. 225–237, 2016.
- [27] D. K. Jones, *Diffusion MRI*. Oxford University Press, 2010.

- [28] P. S. Hüppi, S. E. Maier, S. Peled, G. P. Zientara, P. D. Barnes, F. A. Jolesz, and J. J. Volpe, "Microstructural development of human newborn cerebral white matter assessed in vivo by diffusion tensor magnetic resonance imaging," *Pediatric research*, vol. 44, no. 4, p. 584, 1998.
- [29] J. Dubois, G. Dehaene-Lambertz, S. Kulikova, C. Poupon, P. S. Hüppi, and L. Hertz-Pannier, "The early development of brain white matter: a review of imaging studies in fetuses, newborns and infants," *Neuroscience*, vol. 276, pp. 48–71, 2014.
- [30] K. M. Huynh, T. Xu, Y. Wu, G. Chen, K.-H. Thung, H. Wu, W. Lin, D. Shen, P.-T. Yap, and the UNC/UMN Baby Connectome Project Consortium, "Probing brain micro-architecture by orientation distribution invariant identification of diffusion compartments," in *Medical Image Computing and Computer-Assisted Intervention (MICCAI)*, 2019, pp. 547–555.
- [31] A. W. Anderson, "Measurement of fiber orientation distributions using high angular resolution diffusion imaging," *Magnetic Resonance in Medicine*, vol. 54, no. 5, pp. 1194–1206, 2005.
- [32] Y. Wu, Y. Feng, D. Shen, and P.-T. Yap, "A multi-tissue global estimation framework for asymmetric fiber orientation distributions," in *International Conference on Medical Image Computing and Computer-Assisted Intervention*. Springer, 2018, pp. 45–52.
- [33] H. Zou and T. Hastie, "Regularization and variable selection via the elastic net," *Journal of the Royal Statistical Society: Series B (Statistical Methodology)*, vol. 67, no. 2, pp. 301–320, 2005.
- [34] D. L. Bihan, "Molecular diffusion, tissue microdynamics and microstructure," *NMR in Biomedicine*, vol. 8, no. 7, pp. 375–386, 1995.
- [35] S. N. Jespersen, C. D. Kroenke, L. Østergaard, J. J. Ackerman, and D. A. Yablonskiy, "Modeling dendrite density from magnetic resonance diffusion measurements," *NeuroImage*, vol. 34, pp. 1473–1486, 2007.
- [36] Y. Assaf, R. Z. Freidlin, G. K. Rohde, and P. J. Basser, "New modeling and experimental framework to characterize hindered and restricted water diffusion in brain white matter," *Magnetic Resonance in Medicine*, vol. 52, no. 5, pp. 965–978, 2004.
- [37] O. Pasternak, N. Sochen, Y. Gur, N. Intrator, and Y. Assaf, "Free water elimination and mapping from diffusion MRI," *Magnetic Resonance in Medicine: An Official Journal of the International Society for Magnetic Resonance in Medicine*, vol. 62, no. 3, pp. 717–730, 2009.
- [38] F. Szczepankiewicz, S. Lasič, D. van Westen, P. C. Sundgren, E. Englund, C.-F. Westin, F. Ståhlberg, J. Lätt, D. Topgaard, and M. Nilsson, "Quantification of microscopic diffusion anisotropy disentangles effects of orientation dispersion from microstructure: applications in healthy volunteers and in brain tumors," *NeuroImage*, vol. 104, pp. 241–252, 2015.
- [39] J. Cohen-Adad, M. Descoteaux, S. Rossignol, R. D. Hoge, R. Deriche, and H. Benali, "Detection of multiple pathways in the spinal cord using q-ball imaging," *Neuroimage*, vol. 42, no. 2, pp. 739–749, 2008.
- [40] C. G. Koay, E. Özarslan, and P. J. Basser, "A signal transformational framework for breaking the noise floor and its applications in MRI," *Journal of Magnetic Resonance*, vol. 197, no. 2, pp. 108–119, 2009.
- [41] D. C. Van Essen, S. M. Smith, D. M. Barch, T. E. Behrens, E. Yacoub, and K. Ugurbil, "The WU-Minn human connectome project: An overview," *NeuroImage*, vol. 80, pp. 62–79, 2013.
- [42] B. R. Howell, M. A. Styner, W. Gao, P.-T. Yap, L. Wang, K. Baluyot, E. Yacoub, G. Chen, T. Potts, A. Salzwedel, G. Li, J. H. Gilmore, J. Piven, J. K. Smith, D. Shen, K. Ugurbil, H. Zhu, W. Lin, and J. T. Elison, "The UNC/UMN Baby Connectome Project (BCP): An overview of the study design and protocol development," *NeuroImage*, 2018.
- [43] M. Bergamino, O. Pasternak, M. Farmer, M. E. Shenton, and J. P. Hamilton, "Applying a free-water correction to diffusion imaging data uncovers stress-related neural pathology in depression," *NeuroImage: Clinical*, vol. 10, pp. 336–342, 2016.
- [44] P. Mukherjee, J. H. Miller, J. S. Shimony, T. E. Conturo, B. C. Lee, C. R. Alml, and R. C. McKinstry, "Normal brain maturation during childhood: developmental trends characterized with diffusion-tensor mr imaging," *Radiology*, vol. 221, no. 2, pp. 349–358, 2001.
- [45] K. Lövblad, J. Schneider, K. Ruoss, M. Steinlin, C. Fusch, and G. Schroth, "Isotropic apparent diffusion coefficient mapping of postnatal cerebral development," *Neuroradiology*, vol. 45, no. 6, pp. 400–403, 2003.
- [46] S. Singhi, N. Ganguli, O. Bhakoo, K. Dhall, V. Sood, and A. Kaur, "Body water distribution in newborn infants appropriate for gestational age." *The Indian journal of medical research*, vol. 101, pp. 193–200, 1995.
- [47] K. P. Forbes, J. G. Pipe, and C. R. Bird, "Changes in brain water diffusion during the 1st year of life," *Radiology*, vol. 222, no. 2, pp. 405–409, 2002.
- [48] S. N. Sotiropoulos, S. Moeller, S. Jbabdi, J. Xu, J. L. Andersson, E. J. Auerbach, E. Yacoub, D. Feinberg, K. Setsompop, L. L. Wald, T. E. J. Behrens, K. Ugurbil, and C. Lenglet, "Effects of image reconstruction on fiber orientation mapping from multichannel diffusion MRI: Reducing the noise floor using SENSE," *Magnetic Resonance in Medicine*, vol. 70, pp. 1682–1689, 2013.
- [49] J. M. Guerrero, N. Adluru, B. B. Bendlin, H. H. Goldsmith, S. M. Schaefer, R. J. Davidson, S. R. Kecksemeti, H. Zhang, and A. L. Alexander, "Optimizing the intrinsic parallel diffusivity in NODDI: An extensive empirical evaluation," *PLoS one*, vol. 14, no. 9, 2019.
- [50] M. L. Barr, *The human nervous system: An anatomical viewpoint*. Harper & Row, 1974.
- [51] H. Blumenfeld, *Neuroanatomy through clinical cases*, 2nd ed. Oxford University Press, 2010.
- [52] M. Palombo, A. Ianus, D. Nunes, M. Guerreri, D. C. Alexander, N. Shemesh, and H. Zhang, "SANDI: a compartment-based model for non-invasive apparent soma and neurite imaging by diffusion MRI," *arXiv preprint arXiv:1907.02832*, 2019.
- [53] K. M. Huynh, Y. Wu, K.-H. Thung, S. Ahmad, H. P. Taylor IV, D. Shen, and P.-T. Yap, "Characterizing intra-soma diffusion with spherical mean spectrum imaging," in *Medical Image Computing and Computer-Assisted Intervention (MICCAI)*, 2020.
- [54] H. Sakuma, Y. Nomura, K. Takeda, T. Tagami, T. Nakagawa, Y. Tamagawa, Y. Ishii, and T. Tsukamoto, "Adult and neonatal human brain: diffusional anisotropy and myelination with diffusion-weighted MR imaging," *Radiology*, vol. 180, no. 1, pp. 229–233, 1991.
- [55] D. M. Wimberger, T. P. Roberts, A. J. Barkovich, L. M. Prayer, M. E. Moseley, and J. Kucharczyk, "Identification of 'premyelination' by diffusion-weighted

- MRI.” *Journal of computer assisted tomography*, vol. 19, no. 1, pp. 28–33, 1995.
- [56] C. Lebel, S. Treit, and C. Beaulieu, “A review of diffusion MRI of typical white matter development from early childhood to young adulthood,” *NMR in Biomedicine*, p. e3778, 2017.
- [57] H. Huang, J. Zhang, S. Wakana, W. Zhang, T. Ren, L. J. Richards, P. Yarowsky, P. Donohue, E. Graham, P. C. van Zijl, and S. Mori, “White and gray matter development in human fetal, newborn and pediatric brains,” *Neuroimage*, vol. 33, no. 1, pp. 27–38, 2006.
- [58] M. Cottaar, F. Szczepankiewicz, M. Bastiani, M. Hernandez-Fernandez, S. N. Sotiropoulos, M. Nilsson, and S. Jbabdi, “Accurate fibre dispersion from multiple diffusion encoding,” *arXiv preprint arXiv:1901.05820*, 2019.
- [59] A. F. Howard, J. Mollink, M. Kleinnijenhuis, M. Pallegage-Gamarallage, M. Bastiani, M. Cottaar, K. L. Miller, and S. Jbabdi, “Joint modelling of diffusion MRI and microscopy,” *bioRxiv*, p. 563809, 2019.
- [60] F. Szczepankiewicz, “Imaging diffusional variance by MRI: The role of tensor-valued diffusion encoding and tissue heterogeneity,” Ph.D. dissertation, Lund University, 2016.
- [61] C.-F. Westin, F. Szczepankiewicz, O. Pasternak, E. Özarslan, D. Topgaard, H. Knutsson, and M. Nilsson, “Measurement tensors in diffusion MRI: generalizing the concept of diffusion encoding,” in *International conference on medical image computing and computer-assisted intervention*. Springer, 2014, pp. 209–216.
- [62] C. Ye, “Tissue microstructure estimation using a deep network inspired by a dictionary-based framework,” *Medical image analysis*, vol. 42, pp. 288–299, 2017.
- [63] K. M. Huynh, Y. Wu, K.-H. Thung, S. Ahmad, H. P. Taylor IV, W. Lin, P.-T. Yap, and the UNC/UMN Baby Connectome Project Consortium, “Multivariate quantification of brain development during the first two years of life with mahalanobis distance based on microstructure features,” in *Proceedings of the Annual Meeting of the Organization for Human Brain Mapping (OHBM)*, 2020.
- [64] K. M. Huynh, Y. Wu, K.-H. Thung, S. Ahmad, Z. Wu, G. Li, W. Lin, P.-T. Yap, and the UNC/UMN Baby Connectome Project Consortium, “Densely mapping cortical micro-architecture properties of the developing brain,” in *Proceedings of the Annual Meeting of the Organization for Human Brain Mapping (OHBM)*, 2020.

APPENDIX

Linear Independence

For $b \geq 0$ and $\lambda_{\parallel} \geq \lambda_{\perp} \geq 0$, given

$$h_b(x, \lambda_{\parallel}, \lambda_{\perp}) = \exp(-b\lambda_{\perp}) \exp(-b(\lambda_{\parallel} - \lambda_{\perp})x^2) \quad (S1)$$

and

$$\bar{h}_b(\lambda_{\parallel}, \lambda_{\perp}) = \int_0^1 h_b(x, \lambda_{\parallel}, \lambda_{\perp}) dx, \quad (S2)$$

prove that $\bar{h}_b(\lambda_{\parallel_i}, \lambda_{\perp_i})$ for $i = 1, \dots, n$ are linearly independent with each other with $(\lambda_{\parallel_i} \neq \lambda_{\parallel_j} \vee \lambda_{\perp_i} \neq \lambda_{\perp_j})$ for all $i \neq j$.

Proof. Given

$$\sum_{i=1}^n \mu_i \bar{h}_b(\lambda_{\parallel_i}, \lambda_{\perp_i}) = 0. \quad (S3)$$

We move the term with $\mu_i \geq 0$ to the left and $\mu_i \leq 0$ to the right and rewrite (S3) as

$$\sum_{i=1}^{n_1} \mu_i \bar{h}_b(\lambda_{\parallel_i}, \lambda_{\perp_i}) = \sum_{j=1}^{n_2} \gamma_j \bar{h}_b(\tilde{\lambda}_{\parallel_j}, \tilde{\lambda}_{\perp_j}). \quad (S4)$$

where μ_i, γ_j are all non-negative.

As long as we can show any of the μ_i or γ_j is zero then we can finish the proof by induction. Throughout the proof, we add an indicator (***) when reaching this terminal condition.

Let $\lambda_1 = \min(\{\lambda_{\perp_i} : i = 1, \dots, n_1\})$ and $\lambda_2 = \min(\{\tilde{\lambda}_{\perp_j} : j = 1, \dots, n_2\})$.

Case 1. $\lambda_1 \neq \lambda_2$, W.L.O.G, suppose $\lambda_1 < \lambda_2$

Dividing (S4) by $\frac{\exp(-b\lambda_1)}{\sqrt{b}}$ yield

$$\begin{aligned} & \sum_{\{i:\lambda_{\perp_i}=\lambda_1\}} \mu_i \int_0^1 \sqrt{b} e^{-b(\lambda_{\parallel_i}-\lambda_{\perp_i})x^2} dx + \sum_{\{i:\lambda_{\perp_i}>\lambda_1\}} \mu_i e^{-b(\lambda_{\perp_i}-\lambda_1)} \int_0^1 \sqrt{b} e^{-b(\lambda_{\parallel_i}-\lambda_{\perp_i})x^2} dx \\ &= \sum_{j=1}^{n_2} \gamma_j e^{-b(\tilde{\lambda}_{\perp_j}-\lambda_1)} \int_0^1 \sqrt{b} e^{-b(\lambda_{\parallel_j}-\lambda_{\perp_j})x^2} dx \end{aligned} \quad (S5)$$

Note that

$$\lim_{b \rightarrow \infty} \int_0^1 \sqrt{b} e^{-b(\lambda_{\parallel}-\lambda_{\perp})x^2} dx = \lim_{b \rightarrow \infty} \frac{\pi \operatorname{erf}(\sqrt{b(\lambda_{\parallel}-\lambda_{\perp})})}{2\sqrt{(\lambda_{\parallel}-\lambda_{\perp})}} = \frac{\pi}{2\sqrt{(\lambda_{\parallel}-\lambda_{\perp})}} \neq 0 \quad (S6)$$

where $\operatorname{erf}(\cdot)$ is the error function.

Thus, take $b \rightarrow \infty$, the left hand side goes to a non-zero value while the right hand side goes to zero. This implies that $\mu_i = 0$ for $\{i : \lambda_{\perp_i} = \lambda_1\}$ (***)

Case 2. $\lambda_1 = \lambda_2$, multiply (S4) by $\sqrt{b} \exp(b\lambda_1)$ and take the derivative:

$$\begin{aligned} & \sum_{i=1}^{n_1} \mu_i \left(\frac{1}{2\sqrt{b}} e^{-b(\lambda_{\parallel_i}-\lambda_1)} - \sqrt{b}(\lambda_{\perp_i} - \lambda_1) e^{-b(\lambda_{\perp_i}-\lambda_1)} \int_0^1 e^{-b(\lambda_{\parallel_i}-\lambda_{\perp_i})x^2} dx \right) \\ &= \sum_{j=1}^{n_2} \gamma_j \left(\frac{1}{2\sqrt{b}} e^{-b(\tilde{\lambda}_{\parallel_j}-\lambda_1)} - \sqrt{b}(\tilde{\lambda}_{\perp_j} - \lambda_1) e^{-b(\tilde{\lambda}_{\perp_j}-\lambda_1)} \int_0^1 e^{-b(\tilde{\lambda}_{\parallel_j}-\tilde{\lambda}_{\perp_j})x^2} dx \right) \end{aligned} \quad (S7)$$

rewrite as

$$\begin{aligned} & \sum_{\{i:\lambda_{\perp_i}=\lambda_1\}} \mu_i \frac{1}{2\sqrt{b}} e^{-b\lambda_{\parallel_i}} + \sum_{\{i:\lambda_{\perp_i}>\lambda_1\}} \mu_i \frac{1}{2\sqrt{b}} e^{-b\lambda_{\parallel_i}} + \sum_{\{j:\tilde{\lambda}_{\perp_j}>\lambda_1\}} \gamma_j \sqrt{b}(\tilde{\lambda}_{\perp_j} - \lambda_1) e^{-b\tilde{\lambda}_{\perp_j}} \int_0^1 e^{-b(\tilde{\lambda}_{\parallel_j}-\tilde{\lambda}_{\perp_j})x^2} dx \\ &= \sum_{\{j:\tilde{\lambda}_{\perp_j}=\lambda_1\}} \gamma_j \frac{1}{2\sqrt{b}} e^{-b\tilde{\lambda}_{\parallel_j}} + \sum_{\{j:\tilde{\lambda}_{\perp_j}>\lambda_1\}} \gamma_j \frac{1}{2\sqrt{b}} e^{-b\tilde{\lambda}_{\parallel_j}} + \sum_{\{i:\lambda_{\perp_i}>\lambda_1\}} \mu_i \sqrt{b}(\lambda_{\perp_i} - \lambda_1) e^{-b\lambda_{\perp_i}} \int_0^1 e^{-b(\lambda_{\parallel_i}-\lambda_{\perp_i})x^2} dx. \end{aligned} \quad (S8)$$

Denote $\lambda_{11} = \min(\{\lambda_{\parallel_i} : i = 1, \dots, n_1\} \cup \{\tilde{\lambda}_{\perp_j} : \tilde{\lambda}_{\perp_j} > \lambda_1\})$, the minimum of exponent on the left and $\lambda_{21} = \min(\{\tilde{\lambda}_{\parallel_j} : j = 1, \dots, n_2\} \cup \{\lambda_{\perp_i} : \lambda_{\perp_i} > \lambda_1\})$, the minimum of exponent on the right. We also denote $A_1 = \{\lambda_{\parallel_i} : \lambda_{\perp_i} = \lambda_1\}$, $A_2 = \{\lambda_{\parallel_i} : \lambda_{\perp_i} > \lambda_1\}$, $A_3 = \{\tilde{\lambda}_{\perp_j} : \tilde{\lambda}_{\perp_j} > \lambda_1\}$, $B_1 = \{\tilde{\lambda}_{\parallel_j} : \tilde{\lambda}_{\perp_j} = \lambda_1\}$, $B_2 = \{\tilde{\lambda}_{\parallel_j} : \tilde{\lambda}_{\perp_j} > \lambda_1\}$, $B_3 = \{\lambda_{\perp_i} : \lambda_{\perp_i} > \lambda_1\}$, $M_1 = \{i : \lambda_{\perp_i} > \lambda_1\}$, $N_1 = \{j : \tilde{\lambda}_{\perp_j} > \lambda_1\}$.

Subcase (i): $M_1 \equiv N_1 \equiv \emptyset$, (S8) becomes

$$\sum_{\{i: \lambda_{\perp i} = \lambda_1\}} \mu_i \frac{1}{2\sqrt{b}} e^{-b\lambda_{\parallel i}} = \sum_{\{j: \tilde{\lambda}_{\perp j} = \lambda_1\}} \gamma_j \frac{1}{2\sqrt{b}} e^{-b\tilde{\lambda}_{\parallel j}}. \quad (\text{S9})$$

Since $(A_1 \cap B_1) \equiv \emptyset$, $\lambda_{11} \neq \lambda_{21}$. W.L.O.G, suppose $\lambda_{11} < \lambda_{21}$. Dividing (S9) by $\frac{\exp(-b\lambda_{11})}{\sqrt{b}}$ yields

$$\sum_{\{i: \lambda_{\perp i} = \lambda_1\}} \mu_i \frac{1}{2} e^{-b(\lambda_{\parallel i} - \lambda_{11})} = \sum_{\{j: \tilde{\lambda}_{\perp j} = \lambda_1\}} \gamma_j \frac{1}{2} e^{-b(\tilde{\lambda}_{\parallel j} - \lambda_{11})}. \quad (\text{S10})$$

Take $b \rightarrow \infty$, the left hand side goes to a non-zero value while the right hand side goes to zero. This implies that $\mu_i = 0$ for $\{i: \lambda_{\parallel i} = \lambda_{11}\}$ ($\star \star \star$).

Subcase (ii): Only $M_1 \equiv \emptyset$ or $N_1 \equiv \emptyset$, say $N_1 \equiv \emptyset$, (S8) becomes

$$\begin{aligned} & \sum_{\{i: \lambda_{\perp i} = \lambda_1\}} \mu_i \frac{1}{2\sqrt{b}} e^{-b\lambda_{\parallel i}} + \sum_{\{i: \lambda_{\perp i} > \lambda_1\}} \mu_i \frac{1}{2\sqrt{b}} e^{-b\lambda_{\parallel i}} \\ &= \sum_{\{j: \tilde{\lambda}_{\perp j} = \lambda_1\}} \gamma_j \frac{1}{2\sqrt{b}} e^{-b\tilde{\lambda}_{\parallel j}} + \sum_{\{i: \lambda_{\perp i} > \lambda_1\}} \mu_i \sqrt{b} (\lambda_{\perp i} - \lambda_1) e^{-b\lambda_{\perp i}} \int_0^1 e^{-b(\lambda_{\parallel i} - \lambda_{\perp i})x^2} dx \end{aligned} \quad (\text{S11})$$

- If $\lambda_{11} \neq \lambda_{21}$, say $\lambda_{11} < \lambda_{21}$. Dividing (S11) by $\frac{\exp(-b\lambda_{11})}{\sqrt{b}}$ and taking $b \rightarrow \infty$, the left hand side goes to a non-zero value while the right hand side goes to zero. It implies that $\mu_i = 0$ for $\{i: \lambda_{\parallel i} = \lambda_{11}\}$ ($\star \star \star$).
- If $\lambda_{11} = \lambda_{21}$
Check whether $\lambda_{11} \in A_2$.
 - If $\lambda_{11} \in A_2$, we then have $\lambda_{11} \in B_3$. This is because $\lambda_{11} \in A_2$ implies that there exists i such that $\lambda_{\parallel i} = \lambda_{11}$. We also have $\lambda_{\perp i} \geq \lambda_{11}$ and $\lambda_{\perp i} \geq \lambda_{\parallel i}$. Combine all these three facts and we have $\lambda_{\perp i} = \lambda_{\parallel i}$. Dividing (S11) by $\exp(-b\lambda_{11})$ and taking $b \rightarrow \infty$, the left hand side goes to zero and the right hand side goes to infinity. This implies that $\mu_i = 0$ ($\star \star \star$).
 - If $\lambda_{11} \notin A_2$, we then have $\lambda_{11} \in A_1$ and $\lambda_{11} \in B_3$. Dividing (S11) by $\exp(-b\lambda_{11})$ and taking $b \rightarrow \infty$, the left hand side goes to zero while the right hand side goes to a positive value. This implies that $\mu_i = 0$ for $\{i: \lambda_{\perp i} = \lambda_{11}\}$ ($\star \star \star$).

Subcase (iii): $M_1 \neq \emptyset$ and $N_1 \neq \emptyset$.

- If $\lambda_{11} \neq \lambda_{21}$, say $\lambda_{11} < \lambda_{21}$
Dividing (S8) by $\frac{\exp(-b\lambda_{11})}{\sqrt{b}}$ and taking $b \rightarrow \infty$, the left hand side goes to a non-zero value or infinity while the right hand side goes to zero. It implies that $\mu_i = 0$ for $\{i: \lambda_{\parallel i} = \lambda_{11}\}$ ($\star \star \star$).
- If $\lambda_{11} = \lambda_{21}$, consider
 - $\lambda_{11} \in A_2$ or $\lambda_{11} \in B_2$. Thus $\lambda_{11} \notin (A_2 \cap B_2)$ since there exist i and j that $\lambda_{\perp i} = \lambda_{\parallel i} = \tilde{\lambda}_{\perp j} = \tilde{\lambda}_{\parallel j} = \lambda_{11}$, which is contradictory with $(\lambda_{\parallel i} \neq \tilde{\lambda}_{\parallel j} \vee \lambda_{\perp i} \neq \tilde{\lambda}_{\perp j})$ for all $i \neq j$.
Suppose $\lambda_{11} \in A_2$, then $\lambda_{\perp i} = \lambda_{\parallel i}$ for some i . Dividing (S8) by $\exp(-b\lambda_{11})$ and taking $b \rightarrow \infty$, the left hand side goes to zero while the right hand side goes to infinity. It implies that $\mu_i = 0$ ($\star \star \star$).
 - $\lambda_{11} \notin A_2$, $\lambda_{11} \notin B_2$, and $(\lambda_{11} \in A_1 \text{ or } \lambda_{11} \in B_1)$.
Since $A_1 \cap B_1 = \emptyset$, suppose $\lambda_{11} \in A_1$ and then $\lambda_{11} \in B_3$ on the right hand side only.
 - If $\lambda_{11} \notin A_3$
Dividing (S8) by $\exp(-b\lambda_{11})$ and taking $b \rightarrow \infty$, the left hand side goes to zero while the right hand side goes to a positive value. It implies that $\mu_i = 0$, for $\{i: \lambda_{\perp i} = \lambda_{11}\}$ ($\star \star \star$).
 - If $\lambda_{11} \in A_3$

Divide the equation (S8) by $\exp(-b\lambda_{11})$ and take derivative

$$\begin{aligned}
& \sum_{\{i:\lambda_{\perp i}=\lambda_1, \lambda_{\parallel i}=\lambda_{11}\}} -\mu_i \frac{1}{4b^{\frac{3}{2}}} + \sum_{\{i:\lambda_{\perp i} \geq \lambda_1, \lambda_{\parallel i} > \lambda_{11}\}} \mu_i e^{-b(\lambda_{\parallel i} - \lambda_{11})} \left(-\frac{\lambda_{\parallel i} - \lambda_{11}}{2\sqrt{b}} - \frac{1}{4b^{\frac{3}{2}}}\right) \\
& + \sum_{\{j:\tilde{\lambda}_{\perp j} > \lambda_1\}} \gamma_j (\tilde{\lambda}_{\perp j} - \lambda_1) \frac{1}{2\sqrt{b}} e^{-b(\tilde{\lambda}_{\parallel j} - \lambda_{11})} \\
& - \sum_{\{j:\tilde{\lambda}_{\perp j} > \lambda_{11}\}} \gamma_j (\tilde{\lambda}_{\perp j} - \lambda_1) \sqrt{b} (\tilde{\lambda}_{\perp j} - \lambda_{11}) e^{-b(\tilde{\lambda}_{\perp j} - \lambda_{11})} \int_0^1 e^{-b(\tilde{\lambda}_{\parallel j} - \tilde{\lambda}_{\perp j})x^2} dx \\
& = \sum_{\{j:\tilde{\lambda}_{\perp j} \geq \lambda_1\}} \gamma_j e^{-b(\tilde{\lambda}_{\parallel j} - \lambda_{11})} \left(-\frac{\tilde{\lambda}_{\parallel j} - \lambda_{11}}{2\sqrt{b}} - \frac{1}{4b^{\frac{3}{2}}}\right) \\
& + \sum_{\{i:\lambda_{\perp i} > \lambda_1\}} \mu_i (\lambda_{\perp i} - \lambda_1) \frac{1}{2\sqrt{b}} e^{-b(\lambda_{\parallel i} - \lambda_{11})} \\
& - \sum_{\{i:\lambda_{\perp i} > \lambda_{11}\}} \mu_i (\lambda_{\perp i} - \lambda_1) \sqrt{b} (\lambda_{\perp i} - \lambda_{11}) e^{-b(\lambda_{\perp i} - \lambda_{11})} \int_0^1 e^{-b(\lambda_{\parallel i} - \lambda_{\perp i})x^2} dx
\end{aligned} \tag{S12}$$

Multiplying (S12) by $b^{\frac{3}{2}}$ and taking $b \rightarrow \infty$, the left hand side goes to a non-zero value while the right hand side goes to zero. It implies that $\mu_i = 0$ for $\{i : \lambda_{\perp i} = \lambda_1, \lambda_{\parallel i} = \lambda_{11}\}$ ($\star \star \star$).

- $\lambda_{11} \notin A_1$, $\lambda_{11} \notin A_2$, and $\lambda_{11} \in A_3$. $\lambda_{11} \notin B_1$, $\lambda_{11} \notin B_2$, and $\lambda_{11} \in B_3$.

Multiply (S8) by $\sqrt{b} \exp(b\lambda_{11})$ and take derivative

$$\begin{aligned}
& \sum_{\{i:\lambda_{\perp i} \geq \lambda_1\}} \mu_i e^{-b(\lambda_{\parallel i} - \lambda_{11})} \left(-\frac{\lambda_{\parallel i} - \lambda_{11}}{2\sqrt{b}} - \frac{1}{4b^{\frac{3}{2}}}\right) + \sum_{\{j:\tilde{\lambda}_{\perp j} > \lambda_1\}} \gamma_j (\tilde{\lambda}_{\perp j} - \lambda_1) \frac{1}{2\sqrt{b}} e^{-b(\tilde{\lambda}_{\parallel j} - \lambda_{11})} \\
& - \sum_{\{j:\tilde{\lambda}_{\perp j} > \lambda_{11}\}} \gamma_j (\tilde{\lambda}_{\perp j} - \lambda_1) \sqrt{b} (\tilde{\lambda}_{\perp j} - \lambda_{11}) e^{-b(\tilde{\lambda}_{\perp j} - \lambda_{11})} \int_0^1 e^{-b(\tilde{\lambda}_{\parallel j} - \tilde{\lambda}_{\perp j})x^2} dx \\
& = \sum_{\{j:\tilde{\lambda}_{\perp j} \geq \lambda_1\}} \gamma_j e^{-b(\tilde{\lambda}_{\parallel j} - \lambda_{11})} \left(-\frac{\tilde{\lambda}_{\parallel j} - \lambda_{11}}{2\sqrt{b}} - \frac{1}{4b^{\frac{3}{2}}}\right) + \sum_{\{i:\lambda_{\perp i} > \lambda_1\}} \mu_i (\lambda_{\perp i} - \lambda_1) \frac{1}{2\sqrt{b}} e^{-b(\lambda_{\parallel i} - \lambda_{11})} \\
& - \sum_{\{i:\lambda_{\perp i} > \lambda_{11}\}} \mu_i (\lambda_{\perp i} - \lambda_1) \sqrt{b} (\lambda_{\perp i} - \lambda_{11}) e^{-b(\lambda_{\perp i} - \lambda_{11})} \int_0^1 e^{-b(\lambda_{\parallel i} - \lambda_{\perp i})x^2} dx
\end{aligned} \tag{S13}$$

Multiply both sides with $\exp(-b\lambda_{11})$ and rearrange

$$\begin{aligned}
& \sum_{\{i:\lambda_{\perp i}=\lambda_1\}} \mu_i e^{-b\lambda_{\parallel i}} \left(\frac{\lambda_{\parallel i} - \lambda_{11}}{2\sqrt{b}} + \frac{1}{4b^{\frac{3}{2}}}\right) \\
& + \sum_{\{i:\lambda_{\perp i}=\lambda_{11}\}} \mu_i e^{-b\lambda_{\parallel i}} \left(\frac{\lambda_{\parallel i} - \lambda_{11} + \lambda_{\perp i} - \lambda_1}{2\sqrt{b}} + \frac{1}{4b^{\frac{3}{2}}}\right) + \sum_{\{i:\lambda_{\perp i} > \lambda_{11}\}} \mu_i e^{-b\lambda_{\parallel i}} \left(\frac{\lambda_{\parallel i} - \lambda_{11} + \lambda_{\perp i} - \lambda_1}{2\sqrt{b}} + \frac{1}{4b^{\frac{3}{2}}}\right) \\
& + \sum_{\{j:\tilde{\lambda}_{\perp j} > \lambda_{11}\}} \gamma_j (\tilde{\lambda}_{\perp j} - \lambda_1) \sqrt{b} (\tilde{\lambda}_{\perp j} - \lambda_{11}) e^{-b\tilde{\lambda}_{\perp j}} \int_0^1 e^{-b(\tilde{\lambda}_{\parallel j} - \tilde{\lambda}_{\perp j})x^2} dx \\
& = \sum_{\{j:\tilde{\lambda}_{\perp j}=\lambda_1\}} \gamma_j e^{-b\tilde{\lambda}_{\parallel j}} \left(\frac{\tilde{\lambda}_{\parallel j} - \lambda_{11}}{2\sqrt{b}} + \frac{1}{4b^{\frac{3}{2}}}\right) \\
& + \sum_{\{j:\tilde{\lambda}_{\perp j}=\lambda_{11}\}} \gamma_j e^{-b\tilde{\lambda}_{\parallel j}} \left(\frac{\tilde{\lambda}_{\parallel j} - \lambda_{11} + \tilde{\lambda}_{\perp j} - \lambda_1}{2\sqrt{b}} + \frac{1}{4b^{\frac{3}{2}}}\right) + \sum_{\{j:\tilde{\lambda}_{\perp j} > \lambda_{11}\}} \gamma_j e^{-b\tilde{\lambda}_{\parallel j}} \left(\frac{\tilde{\lambda}_{\parallel j} - \lambda_{11} + \tilde{\lambda}_{\perp j} - \lambda_1}{2\sqrt{b}} + \frac{1}{4b^{\frac{3}{2}}}\right) \\
& + \sum_{\{i:\lambda_{\perp i} > \lambda_{11}\}} \mu_i (\lambda_{\perp i} - \lambda_1) \sqrt{b} (\lambda_{\perp i} - \lambda_{11}) e^{-b\lambda_{\perp i}} \int_0^1 e^{-b(\lambda_{\parallel i} - \lambda_{\perp i})x^2} dx
\end{aligned} \tag{S14}$$

Denote $\lambda_{12} = \min(\{\lambda_{\parallel i} : i = 1 \cdots n_1\} \cup \{\tilde{\lambda}_{\perp j} : \tilde{\lambda}_{\perp j} > \lambda_{11}\})$, the minimum of exponent on the left and $\lambda_{22} = \min(\{\tilde{\lambda}_{\parallel j} : j = 1 \cdots n_2\} \cup \{\lambda_{\perp i} : \lambda_{\perp i} > \lambda_{11}\})$, the minimum of exponent on the right. We also denote $A_{11} = \{\lambda_{\parallel i} : \lambda_{\perp i} \in \{\lambda_1, \lambda_{11}\}\}$, $A_{21} = \{\lambda_{\parallel i} : \lambda_{\perp i} > \lambda_{11}\}$, $A_{31} = \{\tilde{\lambda}_{\perp j} : \tilde{\lambda}_{\perp j} > \lambda_{11}\}$, $B_{11} = \{\tilde{\lambda}_{\parallel j} : \tilde{\lambda}_{\perp j} \in \{\lambda_1, \lambda_{11}\}\}$, $B_{21} = \{\tilde{\lambda}_{\parallel j} : \tilde{\lambda}_{\perp j} > \lambda_{11}\}$, $B_{31} = \{\lambda_{\perp i} : \lambda_{\perp i} > \lambda_{11}\}$, $M_2 = \{i : \lambda_{\perp i} > \lambda_{11}\}$, $N_2 = \{j : \tilde{\lambda}_{\perp j} > \lambda_{11}\}$.

- If $M_2 = N_2 = \emptyset$, (S14) becomes

$$\begin{aligned} & \sum_{\{i: \lambda_{\perp i} = \lambda_1\}} \mu_i e^{-b\lambda_{\parallel i}} \left(\frac{\lambda_{\parallel i} - \lambda_{11}}{2\sqrt{b}} + \frac{1}{4b^{\frac{3}{2}}} \right) + \sum_{\{i: \lambda_{\perp i} = \lambda_{11}\}} \mu_i e^{-b\lambda_{\parallel i}} \left(\frac{\lambda_{\parallel i} - \lambda_{11} + \lambda_{\perp i} - \lambda_1}{2\sqrt{b}} + \frac{1}{4b^{\frac{3}{2}}} \right) \\ &= \sum_{\{j: \tilde{\lambda}_{\perp j} = \lambda_1\}} \gamma_j e^{-b\tilde{\lambda}_{\parallel j}} \left(\frac{\tilde{\lambda}_{\parallel j} - \lambda_{11}}{2\sqrt{b}} + \frac{1}{4b^{\frac{3}{2}}} \right) + \sum_{\{j: \tilde{\lambda}_{\perp j} = \lambda_{11}\}} \gamma_j e^{-b\tilde{\lambda}_{\parallel j}} \left(\frac{\tilde{\lambda}_{\parallel j} - \lambda_{11} + \tilde{\lambda}_{\perp j} - \lambda_1}{2\sqrt{b}} + \frac{1}{4b^{\frac{3}{2}}} \right) \end{aligned} \quad (\text{S15})$$

‡ If $\lambda_{12} \neq \lambda_{22}$, say $\lambda_{12} < \lambda_{22}$

Dividing (S15) by $\frac{\exp(-b\lambda_{12})}{b^{\frac{3}{2}}}$ and taking $b \rightarrow \infty$, the left hand side goes to a non-zero value while the right hand side goes to zero. It implies that $\mu_i = 0$ for $\{i: \lambda_{\parallel i} = \lambda_{12}\}$ ($\star \star \star$).

‡ If $\lambda_{12} = \lambda_{22}$

We have $\lambda_{12} \in \{\lambda_{\parallel i} : \lambda_{\perp i} = \lambda_1\} \cap \{\tilde{\lambda}_{\parallel j} : \tilde{\lambda}_{\perp j} = \lambda_{11}\}$ or $\lambda_{12} \in \{\lambda_{\parallel i} : \lambda_{\perp i} = \lambda_{11}\} \cap \{\tilde{\lambda}_{\parallel j} : \tilde{\lambda}_{\perp j} = \lambda_1\}$ since $\{\lambda_{\parallel i} : \lambda_{\perp i} = \lambda_1\} \cap \{\tilde{\lambda}_{\perp j} : \tilde{\lambda}_{\perp j} = \lambda_1\} = \{\lambda_{\parallel i} : \lambda_{\perp i} = \lambda_{11}\} \cap \{\tilde{\lambda}_{\perp j} : \tilde{\lambda}_{\perp j} = \lambda_{11}\} = \emptyset$.

Suppose $\lambda_{12} \in \{\lambda_{\parallel i} : \lambda_{\perp i} = \lambda_1\} \cap \{\tilde{\lambda}_{\parallel j} : \tilde{\lambda}_{\perp j} = \lambda_{11}\}$ W.L.O.G. Thus, there exist $i_1 \in \{i: \lambda_{\perp i} = \lambda_1\}$ and $j_1 \in \{j: \tilde{\lambda}_{\perp j} = \lambda_{11}\}$ such that $\lambda_{\parallel i_1} = \tilde{\lambda}_{\parallel j_1} = \lambda_{12}$

Dividing (S15) $\exp(-\lambda_{12}b)/\sqrt{b}$ and taking $b \rightarrow \infty$, the left hand side goes to $\mu_{i_1} \frac{\lambda_{\parallel i_1} - \lambda_{11}}{2}$ and the right hand side goes to $\gamma_{j_1} \frac{\tilde{\lambda}_{\parallel j_1} - \lambda_{11} + \tilde{\lambda}_{\perp j_1} - \lambda_1}{2}$. It implies that $\mu_{i_1}(\lambda_{\parallel i_1} - \lambda_{11}) = \gamma_{j_1}(\tilde{\lambda}_{\parallel j_1} - \lambda_{11} + \tilde{\lambda}_{\perp j_1} - \lambda_1)$. With this, (S14) becomes

$$\begin{aligned} & \sum_{\{i: \lambda_{\perp i} = \lambda_1, i \neq i_1\}} \mu_i e^{-b\lambda_{\parallel i}} \left(\frac{\lambda_{\parallel i} - \lambda_{11}}{2\sqrt{b}} + \frac{1}{4b^{\frac{3}{2}}} \right) + \mu_{i_1} e^{-b\lambda_{\parallel i_1}} \frac{1}{4b^{\frac{3}{2}}} \\ &+ \sum_{\{i: \lambda_{\perp i} = \lambda_{11}\}} \mu_i e^{-b\lambda_{\parallel i}} \left(\frac{\lambda_{\parallel i} - \lambda_{11} + \lambda_{\perp i} - \lambda_1}{2\sqrt{b}} + \frac{1}{4b^{\frac{3}{2}}} \right) \\ &= \sum_{\{j: \tilde{\lambda}_{\perp j} = \lambda_1\}} \gamma_j e^{-b\tilde{\lambda}_{\parallel j}} \left(\frac{\tilde{\lambda}_{\parallel j} - \lambda_{11}}{2\sqrt{b}} + \frac{1}{4b^{\frac{3}{2}}} \right) + \gamma_{j_1} e^{-b\tilde{\lambda}_{\parallel j_1}} \frac{1}{4b^{\frac{3}{2}}} \\ &+ \sum_{\{j: \tilde{\lambda}_{\perp j} = \lambda_{11}, j \neq j_1\}} \gamma_j e^{-b\tilde{\lambda}_{\parallel j}} \left(\frac{\tilde{\lambda}_{\parallel j} - \lambda_{11} + \tilde{\lambda}_{\perp j} - \lambda_1}{2\sqrt{b}} + \frac{1}{4b^{\frac{3}{2}}} \right) \end{aligned}$$

Dividing by $\frac{\exp(-b\lambda_{12})}{b^{\frac{3}{2}}}$ and taking $b \rightarrow \infty$, the left hand side goes to $\frac{\mu_{i_1}}{4}$ and the right hand side goes to $\frac{\gamma_{j_1}}{4}$. This implies that

$\mu_{i_1} = \gamma_{j_1}$, which is contradictory with $\mu_{i_1}(\lambda_{\parallel i_1} - \lambda_{11}) = \gamma_{j_1}(\tilde{\lambda}_{\parallel j_1} - \lambda_{11} + \tilde{\lambda}_{\perp j_1} - \lambda_1)$. Thus $\lambda_{12} = \lambda_{22}$ does not happen.

- If $M_1 = \emptyset$ or $N_1 = \emptyset$ only, say $N_2 = \emptyset$

(S14) becomes

$$\begin{aligned} & \sum_{\{i: \lambda_{\perp i} = \lambda_1\}} \mu_i e^{-b\lambda_{\parallel i}} \left(\frac{\lambda_{\parallel i} - \lambda_{11}}{2\sqrt{b}} + \frac{1}{4b^{\frac{3}{2}}} \right) + \sum_{\{i: \lambda_{\perp i} = \lambda_{11}\}} \mu_i e^{-b\lambda_{\parallel i}} \left(\frac{\lambda_{\parallel i} - \lambda_{11} + \lambda_{\perp i} - \lambda_1}{2\sqrt{b}} + \frac{1}{4b^{\frac{3}{2}}} \right) \\ &+ \sum_{\{i: \lambda_{\perp i} > \lambda_{11}\}} \mu_i e^{-b\lambda_{\parallel i}} \left(\frac{\lambda_{\parallel i} - \lambda_{11} + \lambda_{\perp i} - \lambda_1}{2\sqrt{b}} + \frac{1}{4b^{\frac{3}{2}}} \right) \\ &= \sum_{\{j: \tilde{\lambda}_{\perp j} = \lambda_1\}} \gamma_j e^{-b\tilde{\lambda}_{\parallel j}} \left(\frac{\tilde{\lambda}_{\parallel j} - \lambda_{11}}{2\sqrt{b}} + \frac{1}{4b^{\frac{3}{2}}} \right) + \sum_{\{j: \tilde{\lambda}_{\perp j} = \lambda_{11}\}} \gamma_j e^{-b\tilde{\lambda}_{\parallel j}} \left(\frac{\tilde{\lambda}_{\parallel j} - \lambda_{11} + \tilde{\lambda}_{\perp j} - \lambda_1}{2\sqrt{b}} + \frac{1}{4b^{\frac{3}{2}}} \right) \\ &+ \sum_{\{i: \lambda_{\perp i} > \lambda_{11}\}} \mu_i (\lambda_{\perp i} - \lambda_1) \sqrt{b} (\lambda_{\perp i} - \lambda_{11}) e^{-b\lambda_{\perp i}} \int_0^1 e^{-b(\lambda_{\parallel i} - \lambda_{\perp i})x^2} dx \end{aligned} \quad (\text{S16})$$

‡ If $\lambda_{12} \neq \lambda_{22}$, say $\lambda_{12} < \lambda_{22}$

Dividing (S16) by $\frac{\exp(-b\lambda_{12})}{\sqrt{b}}$ and taking $b \rightarrow \infty$, the left hand side goes to a constant while the right hand side goes to zero. It implies that $\mu_i = 0$ for $\{i: \lambda_{\parallel i} = \lambda_{12}\}$ ($\star \star \star$).

‡ If $\lambda_{12} = \lambda_{22}$

Check whether $\lambda_{12} \in A_{21}$.

* If $\lambda_{12} \in A_{21}$

We also have $\lambda_{12} \in B_{31}$. It implies that there exists i such that $\lambda_{\perp i} = \lambda_{\parallel i}$. Dividing (S16) by $\exp(-b\lambda_{12})$ and taking $b \rightarrow \infty$, the left hand side goes to zero while the right hand side goes to infinity. It implies $\mu_i = 0$ ($\star \star \star$).

* If $\lambda_{12} \notin A_{21}$

We next see whether $\lambda_{12} \in B_{31}$.

- If $\lambda_{12} \in B_{31}$, we divide (S16) by $\exp(-b\lambda_{12})$ and take $b \rightarrow \infty$. The left hand side goes to zero while the right hand side goes to infinity. It implies that $\mu_i = 0$ for $\{i : \lambda_{\perp i} = \lambda_{12}\}$ (***)
 - If $\lambda_{12} \notin B_{31}$, we use the same technique when $M_2 = N_2 = \emptyset$ and thus get the contradiction that this case does not exist.
- If $M_2 \neq \emptyset$ and $N_2 \neq \emptyset$.

‡ If $\lambda_{12} \neq \lambda_{22}$, say $\lambda_{12} < \lambda_{22}$

Dividing (S14) by $\frac{\exp(-b\lambda_{12})}{\sqrt{b}}$ and taking $b \rightarrow \infty$, the left hand side goes to a non-zero value or infinity while the right hand side goes to zero. It implies that $\mu_i = 0$ for $\{i : \lambda_{\parallel i} = \lambda_{12}\}$ (***)

‡ If $\lambda_{12} = \lambda_{22}$, consider

* $\lambda_{12} \in A_{21}$ or $\lambda_{12} \in B_{21}$

This is the same with the previous case of $\lambda_{11} \in A_2$ or $\lambda_{11} \in B_2$. We omit the details.

* $\lambda_{12} \notin A_{21}$, $\lambda_{12} \notin B_{21}$, and $(\lambda_{12} \in A_{11}$ or $\lambda_{12} \in B_{11})$.

Here we claim that $\lambda_{12} \notin A_{11} \cap B_{11}$ and everything else is the same with the previous case of $\lambda_{11} \notin A_2$, $\lambda_{11} \notin B_2$, and $(\lambda_{11} \in A_1$ or $\lambda_{11} \in B_1)$.

This is because if $\lambda_{12} \in A_{11} \cap B_{11}$, then we can only have $\lambda_{12} \in \{\lambda_{\parallel i} : \lambda_{\perp i} = \lambda_1\} \cap \{\tilde{\lambda}_{\parallel j} : \tilde{\lambda}_{\perp j} = \lambda_{11}\}$ or $\lambda_{12} \in \{\lambda_{\parallel i} : \lambda_{\perp i} = \lambda_{11}\} \cap \{\tilde{\lambda}_{\parallel j} : \tilde{\lambda}_{\perp j} = \lambda_1\}$ since $\{\lambda_{\parallel i} : \lambda_{\perp i} = \lambda_1\} \cap \{\tilde{\lambda}_{\parallel j} : \tilde{\lambda}_{\perp j} = \lambda_1\} = \emptyset$ and $\{\tilde{\lambda}_{\parallel j} : \tilde{\lambda}_{\perp j} = \lambda_{11}\} \cap \{\lambda_{\parallel i} : \lambda_{\perp i} = \lambda_{11}\} = \emptyset$.

Suppose $\lambda_{12} \in \{\lambda_{\parallel i} : \lambda_{\perp i} = \lambda_1\} \cap \{\tilde{\lambda}_{\parallel j} : \tilde{\lambda}_{\perp j} = \lambda_{11}\}$ W.L.O.G. Then there exist $i_1 \in \{i : \lambda_{\perp i} = \lambda_1\}$ and $j_1 \in \{j : \tilde{\lambda}_{\perp j} = \lambda_{11}\}$ such that $\lambda_{\parallel i_1} = \tilde{\lambda}_{\parallel j_1} = \lambda_{12}$.

We divide (S14) by $\exp(-b\lambda_{12})$ and take derivative; then multiply the result by $b^{\frac{3}{2}}$ and take $b \rightarrow \infty$. The left hand side goes to $-\frac{\mu_{i_1}(\lambda_{\parallel i_1} - \lambda_{11})}{4}$ while the right hand side goes to $-\frac{\gamma_{j_1}(\tilde{\lambda}_{\parallel j_1} - \lambda_{11} + \tilde{\lambda}_{\perp j_1} - \lambda_1)}{4}$, which implies that $\mu_{i_1}(\lambda_{\parallel i_1} - \lambda_{11}) = \gamma_{j_1}(\tilde{\lambda}_{\parallel j_1} - \lambda_{11} + \tilde{\lambda}_{\perp j_1} - \lambda_1)$. Plugging back in (S14) yields

$$\begin{aligned}
& \sum_{\{i: \lambda_{\perp i} = \lambda_1, i \neq i_1\}} \mu_i e^{-b\lambda_{\parallel i}} \left(\frac{\lambda_{\parallel i} - \lambda_{11}}{2\sqrt{b}} + \frac{1}{4b^{\frac{3}{2}}} \right) + \mu_{i_1} e^{-b\lambda_{\parallel i_1}} \left(\frac{1}{4b^{\frac{3}{2}}} \right) \\
& + \sum_{\{i: \lambda_{\perp i} = \lambda_{11}\}} \mu_i e^{-b\lambda_{\parallel i}} \left(\frac{\lambda_{\parallel i} - \lambda_{11} + \lambda_{\perp i} - \lambda_1}{2\sqrt{b}} + \frac{1}{4b^{\frac{3}{2}}} \right) \\
& + \sum_{\{i: \lambda_{\perp i} > \lambda_{11}\}} \mu_i e^{-b\lambda_{\parallel i}} \left(\frac{\lambda_{\parallel i} - \lambda_{11} + \lambda_{\perp i} - \lambda_1}{2\sqrt{b}} + \frac{1}{4b^{\frac{3}{2}}} \right) \\
& + \sum_{\{j: \tilde{\lambda}_{\perp j} > \lambda_{11}\}} \gamma_j (\tilde{\lambda}_{\perp j} - \lambda_1) \sqrt{b} (\tilde{\lambda}_{\perp j} - \lambda_{11}) e^{-b\tilde{\lambda}_{\perp j}} \int_0^1 e^{-b(\tilde{\lambda}_{\parallel j} - \tilde{\lambda}_{\perp j})x^2} dx \\
& = \sum_{\{j: \tilde{\lambda}_{\perp j} = \lambda_1\}} \gamma_j e^{-b\tilde{\lambda}_{\parallel j}} \left(\frac{\tilde{\lambda}_{\parallel j} - \lambda_{11}}{2\sqrt{b}} + \frac{1}{4b^{\frac{3}{2}}} \right) + \gamma_{j_1} e^{-b\tilde{\lambda}_{\parallel j_1}} \left(\frac{1}{4b^{\frac{3}{2}}} \right) \\
& + \sum_{\{j: \tilde{\lambda}_{\perp j} = \lambda_{11}, j \neq j_1\}} \gamma_j e^{-b\tilde{\lambda}_{\parallel j}} \left(\frac{\tilde{\lambda}_{\parallel j} - \lambda_{11} + \tilde{\lambda}_{\perp j} - \lambda_1}{2\sqrt{b}} + \frac{1}{4b^{\frac{3}{2}}} \right) \\
& + \sum_{\{j: \tilde{\lambda}_{\perp j} > \lambda_{11}\}} \gamma_j e^{-b\tilde{\lambda}_{\parallel j}} \left(\frac{\tilde{\lambda}_{\parallel j} - \lambda_{11} + \tilde{\lambda}_{\perp j} - \lambda_1}{2\sqrt{b}} + \frac{1}{4b^{\frac{3}{2}}} \right) \\
& + \sum_{\{i: \lambda_{\perp i} > \lambda_{11}\}} \mu_i (\lambda_{\perp i} - \lambda_1) \sqrt{b} (\lambda_{\perp i} - \lambda_{11}) e^{-b\lambda_{\perp i}} \int_0^1 e^{-b(\lambda_{\parallel i} - \lambda_{\perp i})x^2} dx
\end{aligned} \tag{S17}$$

Again, we divide (S17) by $\exp(-b\lambda_{12})$ and take derivative; then multiply the result by $b^{\frac{5}{2}}$ and take $b \rightarrow \infty$. The left hand side goes to $-\frac{3\mu_{i_1}}{8}$ while the right hand side goes to $-\frac{3\gamma_{j_1}}{8}$, which implies that $\mu_{i_1} = \gamma_{j_1}$. This is contradictory with $\mu_{i_1}(\lambda_{\parallel i_1} - \lambda_{11}) = \gamma_{j_1}(\tilde{\lambda}_{\parallel j_1} - \lambda_{11} + \tilde{\lambda}_{\perp j_1} - \lambda_1)$. Thus, this case does not exist.

* $\lambda_{11} \notin A_1$ and $\lambda_{11} \notin A_{21}$ and $\lambda_{11} \in A_{31}$. $\lambda_{11} \notin B_{11}$ and $\lambda_{11} \notin B_{21}$ and $\lambda_{11} \in B_{31}$.

We multiply (S14) by $\sqrt{b} \exp(b\lambda_{12})$ and take derivative. We then repeatedly follow the same procedures in the previous case of “ $\lambda_{11} \notin A_1$, $\lambda_{11} \notin A_2$, and $\lambda_{11} \in A_3$. $\lambda_{11} \notin B_1$, $\lambda_{11} \notin B_2$, and $\lambda_{11} \in B_3$ ” to finish the proof. \square